Development of an Aptasensor for Detection of Tumour Necrosis Factor Alpha based on Transition Metal Dichalcogenide

by

G. L. Thushani De Silva

M.Sc. (Physics), Southern Illinois University, 2019

B.Sc. (Engineering Physics), University of Colombo, 2014

Thesis Submitted in Partial Fulfillment of the

Requirements for the Degree of

Master of Applied Science

in the

School of Engineering Science

Faculty of Applied Sciences

Copyright © G. L. Thushani De Silva 2022

SIMON FRASER UNIVERSITY

Spring 2022

Copyright in this work is held by the author. Please ensure that any reproduction or re-use is done in accordance with the relevant national copyright legislation.

Declaration of Committee

Name:	**G. L. Thushani De Silva**
Degree:	**Master of Applied Science**
Title:	**Development of an aptasensor for detection of Tumour Necrosis Factor alpha based on transition metal dichalcogenide**
Committee:	**Chair: Shawn Sederberg** Assistant Professor, Engineering Science
	Michael Adachi Supervisor Assistant Professor, Engineering Science
	Karen Kavanagh Committee Member Professor, Physics
	Miriam Rosin Committee Member Professor, Biomedical Physiology and Kinesiology
	Ash Parameswaran Examiner Professor, Engineering Science

Abstract

An abnormal increase in cytokine, a biomolecule found in body fluids, is often an indication of failing health conditions, which has made the early detection of such events of great importance. In this study, an aptameric cytokine sensor was built based on the diode behavior that arises due to asymmetric contact area or length of MoS_2 geometries. For a proof of concept, the sensor was tested for tumor nercosis factor-α (TNF-α), an inflammatory cytokine biomarker. The sensor showed an ultra-sensitive limit of detection (LOD) (compared to many other cytokine sensors at present) of 10 fM for TNF-α, with a good selectivity against IL-6 and C-reactive proteins. This detection is one order of magnitude less than the levels present in blood serums of healthy young adults and is therefore, a good candidate for early diagnosis.

Keywords: Cytokine Sensor; MoS_2; Asymmetric MoS_2 Diode sensor; TNF-α, Aptasensor

Dedication

This thesis is dedicated to my family who has given me their unwavering support through thick and thin! If not for them, I would never be able to realize my dreams which I didn’t even know that I was making.

Acknowledgements

There are many individuals to whom I'm immensely grateful for supporting me throughout this journey. Knowing that I will eventually run out of space while trying to acknowledge them all, I'm still going to try.

First and foremost, I would like to acknowledge the unwavering support given by my supervisor Prof. Michael Adachi. I'm at a loss for words to express my gratitude for him. I have lost count on the occasions I have sought him out with all the problems where he had always guided me to overcome them. It amazes me how he would always find time to help us in his busy schedule, no matter what the issue is.

Thank you so much Prof. Kavanagh for guiding me to apply for the School of Engineering Science. If it was not for you, I wouldn't be able to meet my supervisor. Thank you for allowing us to use your laboratory and equipment whenever needed. Furthermore, I make this an opportunity to acknowledge both Prof. Kavanagh and Prof. Rosin for their continuous guidance and encouragement throughout this journey. Thank you so much for giving me your valuable time when ever I needed your advice.

Thank you, Prof. Parameswaran and Prof. Gray, for giving me many advice and guidance to make this project work. Your wise words helped me to make this project a success. Thank you so much for allowing me to use your tools and equipment whenever I asked and treating me as your student.

Next, I would like to acknowledge my amazing research group though I won't have enough space to mention your contribution individually. You have been immensely supportive during every step of this project, helped me with the lab work, given such great comments and advice and even helped me with device characterization, data measurements and analysis. I feel so lucky to be a part of such a wonderful team. Thank you so much Mirette Fawzy (PhD student, Physics, SFU), Hamidreza Ghanbari (PhD student, ENSC, SFU), Yue Ling (former BASc student, ENSC, SFU), Askar Abdelrahman (PhD student, ENSC, SFU), Dr. Amirhossein Hasani (Postdoc, ENSC, SFU), Amin Abnavi (PhD student, ENSC, SFU), MohammadReza Mohammadzadeh (PhD student, ENSC, SFU), Ribwar Ahmadi (MASc student, ENSC, SFU), Fahmid Kabir (PhD student, ENSC, SFU), Samantha Betts (former BASc student, ENSC, SFU), Bennett Sasaki (former BASc student, ENSC, SFU), Kwok Liang Lee (former BASc student, ENSC, SFU), Dr. Sikandar

Aftab (Postdoc, ENSC, SFU), Bakhtiar Azim (former MASc student, ENSC, SFU) Dr. Peng Wu (former Postdoc, ENSC, SFU), Dr. Rowshan Rahmanian (former Postdoc, ENSC, SFU).

Last but not least, I would like to acknowledge the funding support given by CMC Microsystems, National Sciences and Engineering Research Council of Canada (NSERC), and School of engineering Science at Simon Fraser University (SFU).

Table of Contents

List of Tables

List of Figures

List of Acronyms

Al_2O_3	Aluminum Oxide
ALD	atomic layer deposition
Ar	Argon
Au	Gold
BOE	buffered oxide etchant
CPD	Contact Potential Difference
Cr	Chromium
CVD	Chemical Vapor Deposition
DI water	Deionized Water
DNA	Deoxyribonucleic Acid
FET	Field Effect Transistor
FRET	Fluorescence Resonance Energy Transfer
G-quadruplex	Guanine quadruplex
KP	Kelvin Probe
N_2	Nitrogen
PBS	phosphate-buffered saline
S	Sulfur
SELEX	Systematic Evolution of Ligands by Exponential Enrichment
Si	Silicon
SiO_2	Silicon Dioxide
SMUs	Source Measurement Units
TMD	Transition Metal Dichalcogenides
TNF-α	Tumour Necrosis Factor alpha

Chapter 1. Introduction

1.1. Importance of Biosensors

With the continuous rise of numerous diseases, biosensors have become indispensable for the public health care in the modern society. Particularly diseases like pancreatic cancer, breast cancer etc., can be cured if they are diagnosed at an early stage[1]. One effective method to detect these diseases is by detecting any abnormal increase of biomarkers in body fluids such as blood or in tissues. Particularly, biomarkers such as cytokines have a link to many diseases, which makes the early detection of an abnormal increase of them of great importance[2]. Biosensors consist of a biorecognition element with a transducer, which transforms the interactions between the biorecognition element (the receptor) and the specific target into a measurable signal[3]. This working principle is often used in developing cytokine (target) sensors with aptamers as the receptor. Aptamers, which are short, single-stranded nucleic acid segments have gained more interest as a tool for biosensing due to its ability to bind to a range of biomolecules such as cytokine proteins[4]. Different sensing techniques ranging from optical to resonance frequency to electrochemical/electrical can be used in building biosensors which are immensely beneficial in point-of-care medical testing[5-8].

However, the existing methods to detect cytokines contain several disadvantages such as complexity in sample preparation, high processing time, high cost and possible low sensitivity[1, 2, 9]. Serum levels of tumor nercosis factor-α (TNF-α) concentration among healthy young and adult population is typically in the range of 188 fM to 289 fM[10]. In the case of children, the serum levels can be as low as 12.28 fM[11]. Therefore, for the early detection of abnormal increaser of cytokine level, it is important to develop sensors with detection limits at low fM range. Hence, there is a need for a highly sensitive, selective, simple, and rapid method for the detection of cytokines. In recent years, transition metal dichalcogenides (TMD) (e.g. molybdenum disulfide (MoS_2) and tungsten disulfide (WS_2)) have become a popular choice of material for biosensing applications since they have many properties favorable for building biosensors[12].

1.2. Project Goal

The overall goal of the project was to develop an aptamer based cytokine sensor to detect TNF-α, incorporating an electrical mechanism such as a field effect transistor (FET). There are several sensing materials that can be employed in building cytokine sensors. Among them, 2-D materials such as graphene and TMDs are a popular choice for electrical biosensors due to the convenience of device fabrication and functionalization technique. However, it has been reported that between graphene and MoS_2 based FET biosensors, the sensitivity of the MoS_2 sensor is much higher (74-fold higher)[12]. Therefore, as opposed to graphene, TMD materials such as MoS_2 could be the ultimate option to achieve lower limit of detection (LOD) and high sensitivity.

In this project, we have employed two kinds of TMDs, WS_2 which were synthesized using chemical vapour deposition (CVD) and MoS_2 which were synthesized via mechanical exfoliation. The basic idea was to immobilize aptamers on the surface of the TMD using thiol or amine linkers where the free end has the capability to bind to the targeted cytokine proteins[4, 6]. Since cytokines contain a charge, once they are bound to the aptamers immobilized on the sensing area, the transport property (e.g. the surface current) of the TMD crystal changes significantly[1, 2]. Such changes are often detectable via electrical measurement such as current versus voltage (I-V) measurements which can then be utilized for evaluating the number of cytokines begin bound. Hence our goal is to incorporate this mechanism to develop a cytokine sensor that ultimately could be improved for clinical application.

1.3. The Structure of the Thesis

There were several projects that have been carried out with in the span of 15 months involving quartz crystal microbalance-based gas sensors, quartz crystal microbalance based cytokine sensors and electrical cytokine sensors. However, only the work related to electrical cytokine sensors has been presented in this thesis.

Introduction chapter includes a literature review on biosensors. Various biosensing mechanisms based on optical biosensors, resonator biosensors, and electrochemical and electrical biosensors are presented. Furthermore, a summary of MoS_2 for biosensing application and aptamers as a better receptor for biosensing have been included.

Next chapter covers a summary of synthesis and characterization techniques used during the study. In this chapter, chemical vapor deposition and mechanical exfoliation have been discussed as synthesis techniques. For material characterization techniques, atomic force microscopy, kelvin probe force microscopy, fluorescence spectroscopy and a probe station for electrical measurements have been included.

The following chapter contains the experimental details, results and a discussion incorporating the observations. The initial attempts at developing a field effect transistor (FET) cytokine sensor and final work based on the diode cytokine sensor is discussed in this chapter.

Final chapter includes the conclusions related to findings from chapter 4 and future work in order to improve the cytokine diode sensor is discussed.

Chapter 2. Biosensors

2.1. Optical Biosensors

Optical sensors are customarily based on measuring photoluminescence such as fluorescence, against the biomolecule concentration. For example, a study carried out by Geldert A. et al. illustrates a biosensor developed using MoS_2 nanosheet incorporating a fluorescence resonance energy transfer (FRET) mechanism. A fluorescently-labeled aptamer which has been combined with a fluorescence quenching material to which aptamer were spontaneously adsorbed (hence their fluorescence have been quenched) were employed for the study[4]. Upon the addition of the target, which is a malarial biomarker in their case, the aptamer change its conformation to bind to its target, causing the aptamer to be released from the quencher resulting in a measurable fluorescence increase[4]. Another study carried out by Ghosh S. et al. presented their work on detecting TNF-α using a quantum dot based optical biosensor via FRET mechanism with a LOD in the pM range[13].

The main drawback in optical cytokine sensors is the additional modifications requires during the synthesis to attach the FAM label while a label-free detection mechanism is comparatively cost-effective. Another common drawback is their lower sensitivity which make them unsuitable for detecting cytokine levels in a healthy human since their inability to reach fM detection levels. However, a recent study has illustrated the possibility of detecting a malaria biomarker employing an antibody-aptamer plasmonic biosensor with a LOD ~ 18 fM, but the post measurement image processing requirements make it unfavourable for rapid detection[7].

2.2. Resonator Biosensors

Resonator biosensors work based on the relationship between their mass and the resonance frequency. An accumulation of mass results in a decrease of the resonance frequency[14]. One of the popular sensors which has incorporated resonance frequency mechanism is the quartz crystal microbalance (QCM) sensor. Yao C. et al. reported an aptamer-based QCM biosensor array for the quantification of Immunoglobulin E (IgE) where a clear difference in the resonance frequency was observed as the IgE

concentration was increased[14]. However, similar to many optical cytokine sensors, the QCM sensors have shown a low sensitivity. Hence the applicability of QCM based cytokine sensors for early diagnosis purposes to be inadequate even with the integration of other strategies to improve the sensing ability, such as coupling the resonance frequency to magnetic fields since the LOD for most of the QCM sensors lies in the range of nM [15].

Alternative ideas for nano scale resonators for cytokine detection with high sensitivity has been speculating for some time. However, since the normal methods of vibrative transduction for nanoelectromechanical systems (NEMS) are not suitable for 2D atomic-layer sensors, 2-D nano-resonator-based biosensors have not been reported until recently. A study carried out by Jiang et al. illustrates a nano-resonator which has been constructed by connecting a free-standing MoS_2 monolayer to the source and drain electrodes for a FET[16]. In their study, the assembly and manipulation of single-atomic layer piezo-resonators as mass sensors with eigen mechanical resonances up to gigahertz has been described. The nano-resonators have employed electronic vibration transducers based on piezo-electric polarization charges of monolayer MoS_2. This novel approach is a direct detection method that has reached a high Q-factor and optimal atomic-layer sensor export for detecting single-stranded deoxyribonucleic acid (DNA) [16]. However, since the measurements for cytokine detection are typically carried out in a liquid environment, the high damping factor could have had an adverse effect on the sensitivity making it challenging to reach fM detection limits.

2.3. Electrochemical & Electrical Biosensors

The working principle behind the electrochemical biosensors is based on detecting biological analyte through redox reactions on electrodes[17]. Since a gold (Au) surface reacts with thiol groups, Au nanoparticles are often used as anchoring sites for immobilization of thiol-terminated aptamers as bioreceptors. Su et al. reported a MoS_2-based electrochemical aptasensor for the simultaneous detection of thrombin and adenosine triphosphate [18]. Two different aptamer probes labeled with redox tags were simultaneously immobilized on a] AuNP−MoS_2 film (through Au-thiol bonds)[18]. The sensor was shown to be capable of detecting thrombin concentrations ranging from 0.01nM to 10 μM[18].

Apart from measuring electrochemical redox measurements, there are several studies on biosensors based on electrochemical impedance, electrochemical capacitance and photoelectrochemical detection mechanisms[19-21]. For example, a label-free electrochemical impedance spectroscopy based biosensor has been developed by Arkusz K. at el. for detection of TNF-α with a LOD of 0.29 pM[21]. The sensor was constructed using TiO_2 nanotubes and the receptors (antibodies) were immobilized on the surface using physisorption[21]. Bahri M. et al. has reported a cytokine sensor for the detection of TNF-α based on silicon nitride substrate with a high sensitivity[19]. The capacitance of the sensor was measured as a function of the applied potential[19]. The normalized capacitance response displayed a variation along the cytokine concentration with a 58.5 fM LOD[19]. Another study reported a photoelectrochemical sandwich immunosensor for TNF-α detection by utilizing anti-TNF-α nanobody as the receptor. The performance of the sensor was evaluated by measuring the photocurrent signal change with TNF-α concentration[20].

While electrochemical sensors have displayed a capability of reaching lower detection limits for cytokine detection, their specificity is typically lower compared to electrical sensors such as FET-based biosensors[22, 23]. In a conventional FET, two electrodes, source and drain are connected through a semiconductor material called the channel, which can be a TMD[24]. Current flowing through the channel between the source and drain is electrostatically modulated by a third electrode called the gate, which is capacitively coupled through a dielectric layer. Apart from these main components, a main feature of a FET biosensor is the passivation layer, that minimizes the current leakage through the top electrodes during measurement [24].

Figure 1 shows the schematic diagram of the cross-section of different types of FET device for biosensing. Typically, there are three types of gating seen in FET biosensors, back gating, top gating (without liquid) and liquid gating. Back gating is applied via the substrate, in this case Si where a silicon dioxide (SiO_2) layer acts as the dielectric layer (Figure 1a)). In top gating, there is a dielectric layer, such as aluminum oxide (Al_2O_3) covering the channel region which acts as the dielectric layer for a gate metal layer applied from the top of the channel (Figure 1b)) [25]. The third type is similar to the conventional top gating, but the gate voltage is applied via a liquid drop on the channel using a probe (Figure 1c)).

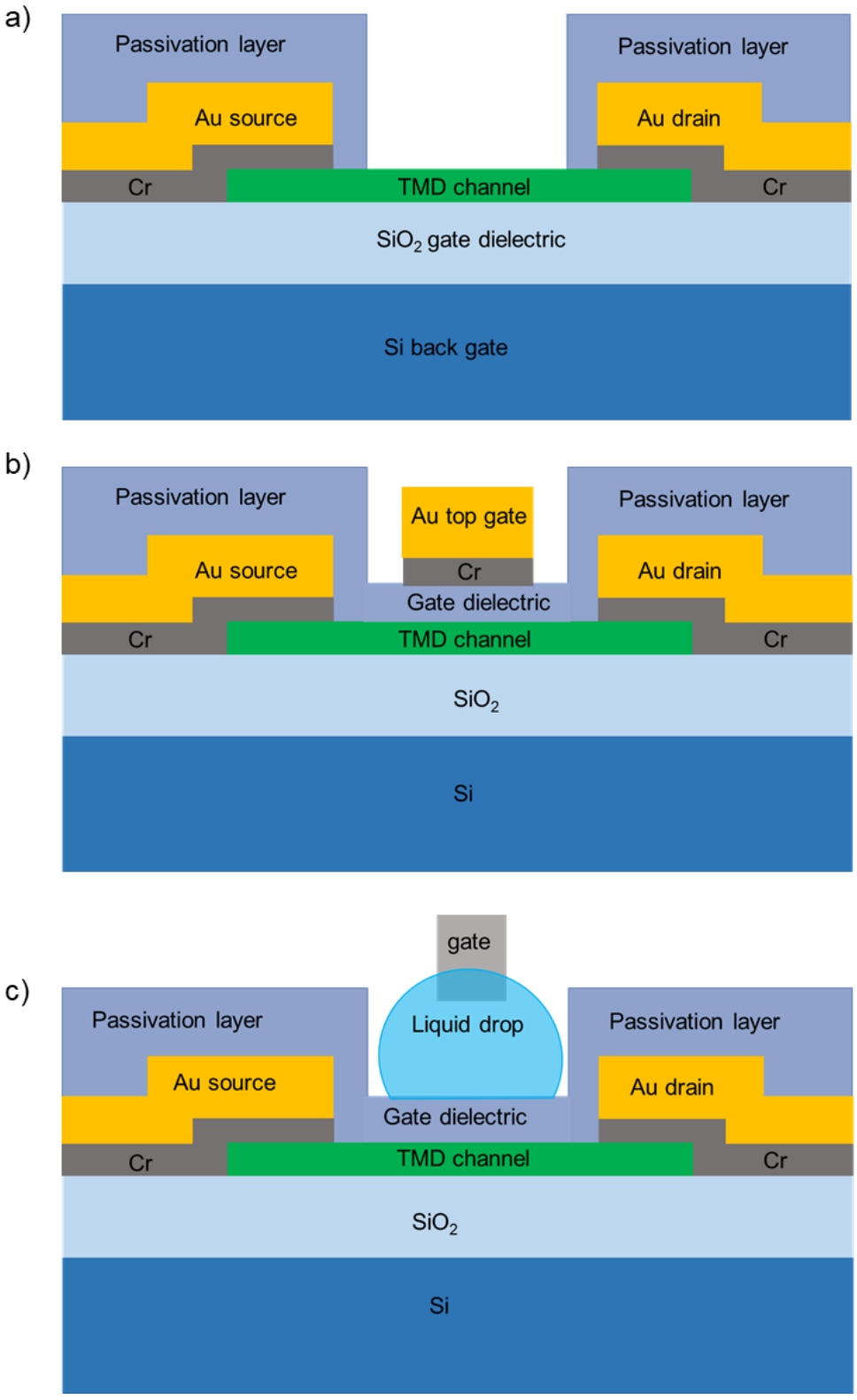

Figure 1: **Cross section diagrams of basic FET biosensors a) back gated b) top gated c) liquid gated.**

Compared to a conventional sensor, a FET sensor can amplify the electrical signals across the channel by applying voltages to the gate electrode [24]. Typically, FET cytokine sensors benefit from their simpler sensing mechanisms and the absence of tedious post measurement data processing. During interaction with the biomolecules, the electrical characteristics of the sensing layer (the channel) in the FET are changed by trapping or doping through target analytes hence giving rise to a measurable change in the electrical response related to the biomolecule concentration [24].

A study has been conducted by Wang L. et al. using a MoS_2 FET with HfO_2 as a dielectric to detect prostate-specific antigen (PSA)) which is a cancer marker[1]. Once the antibodies were attached to the device surface that specifically bind with PSA molecules in the solution, the binding events caused a detectable electrical signal in terms of source-drain current changes according to field-effect mechanism with an almost instant response [1]. Hao Z. et al. reported a graphene-based FET sensor for detection of TNF-α cytokine. The affinity recognition of the biomarker has been realized by a short DNA aptamer. The detection of the cytokine was allowed by the structural change of the aptamer immobilized to the graphene surface, which would change into a guanine quadruplex (G-quadruplex) formation bringing the charged cytokine closer to the graphene surface hence increasing the surface charges on graphene[22]. The graphene FET sensor showed an excellent response to TNF-α concentrations with a LOD at 26 pM [22].Typical FET cytokine sensors that have employed graphene as the sensing material, have reported a high LOD (in pM range). A study carried out by Sarkar D. experimentally illustrated that between graphene and MoS_2 based FET biosensors, the sensitivity of the MoS_2 sensor is much higher (74-fold higher)[12]. In fact, The only FET cytokine sensor to reach the fM LOD for sensing TNF-α has been fabricated employing MoS_2 [26].The serum levels of TNF-α concentration among healthy young and adult population is typically in the range of 188 fM to 289 fM[10]. In the case of children, the serum levels can be as low as 12.28 fM[11]. Hence for early detection of abnormal increaser of cytokine level, it is important to develop sensors with detection limits in the low fM range. Therefore, as opposed to graphene, TMD materials such as MoS_2 could be prefered to achieve lower LOD and higher sensitivity.

2.4. MoS_2 as the Biosensing Layer

MoS_2 and WS_2 are 2-D material that belong to the family of TMDs [27]. Its excellent electron transfer capacity realized by the large number of active sites, large specific area,

and the large surface/volume ratio has made MoS_2 or WS_2 a competitive candidate for biosensor application [28-30]. Due to the existence of the intrinsic bandgap in MoS_2 and WS_2, they have become superior choices of material compared to the zero-bandgap graphene. The absence of a bandgap in graphene usually leads to higher noise particularly in fabrication of transistor-based biosensors. The piezoelectric properties displayed by monolayer TMDs like MoS_2 and WS_2 have also opened doors to exploration of piezoelectric nano-resonators based biosensors. The following table extracted from the study by Sarkar D. et al. illustrates the comparison between MoS_2 and several other competing material for biosensing[12].

Table 1: Comparison of the performance of MoS_2 with several other competing materials for biosensing[12].

Material	Sensitivity	Device Scalability	Flexibility and Transparency
3-D bulk materials	Low	Possible	Low
Silicon nano wires	High	Challenging	Low
Carbon nanotubes	High	Challenging	High
Graphene	Low	High	High
MoS_2	High	High	High

Table 1 compares the sensitivity, device scalability, flexibility and transparency of several biosensing materials. Apart from the sensitivity, device scalability, which can also be termed as the dimension controllability of the sensor is an important parameter to obtain reliable sensors for real-world applications [31]. The flexibility of the sensor means the ability to perform in bent/strained state in a consistent manner so that the devices can be extended to wearable applications [32]. The transparency of a device is helpful to incorporate the sensor with optoelectronic systems for healthcare applications [33].

Functionalization of sensor surfaces using aptamers or antibodies is widely used for developing biosensors [4]. Pristine MoS_2 nanosheets typically contain Sulfur (S) vacancies on its surface. These S vacancy sites prefer to covalently bond with S functional groups such as thiol anchoring groups, where by capturing free electrons, a S atom forms a chemisorbed bond with the S vacancy site of MoS_2 [34]. Hence, aptamers and antibodies

can be easily attached onto the surface of MoS_2 via thiol linkers, making MoS_2 more suitable for biosensing. This immobilization technique can be extended to other TMD materials in family such as WS_2, WSe_2, etc. where the S terminated end of the linker tend to strongly interact with the chalcogenide atoms and preferably vacancy sites on the surface of the TMD[35].

Apart from using thiol-ended anchoring groups, it is also possible to immobilize the receptors using the amine-anchoring groups. The silane chemistry of Glycidoxypropyltrimethoxysilane (GOPS) reaction with Carbonyldiimidazole (CDI) enables the formation of a covalent bond with amine-terminated receptors (aptamer and antibody)[36-38]. In order to facilitate the silane chemistry, the starting surface needs to contain hydroxyl groups which are typically abundant on surfaces such as SiO_2, Al_2O_3, HfO_2 etc.[36] Therefore, for amine-terminated receptors to immobilize on MoS_2, the MoS_2 (or any other TMD) surface needs to be coated with an oxide layer such as SiO_2, Al_2O_3, HfO_2 etc.[39] In fact, these ALD assisted surface modifications, enabled many materials to be functionalized with amine-ended bioreceptors vis silane chemistry.

2.5. Aptamers for biosensing

One of the important components in a biosensor is the biorecognition element, also known as the receptor, that has the capability to bind to the target such as cytokines for sensing purpose. The main two types of bioreceptors employed in biosensors are aptamers which are short, single-stranded nucleic acid oligomers and antibodies. Antibodies, have been in use for over 70 years and are still considered the “gold standard”[40]. Nevertheless, aptamers, also termed “chemical antibodies”, are expected to replace antibodies in the near future due to the possibility of obtaining higher affinity and exquisitely specificity via systematic evolution of ligands by exponential enrichment (SELEX) for a wide range of targets such as small molecules, proteins and whole cells[40-42]. A selected type of an aptamer can be massively synthesized via this chemical process making it more cost-effective than the production of the antibody [42]. Compared to antibodies, aptamers are easily modified chemically for modification of signal moieties such as electrochemical probes, fluorophores and quenchers[42]. Apart from this, aptamers are small in size, highly stable and can display an outstanding performance in complex media[40]. Furthermore aptamers can form diverse complex secondary structures ranging from multi-branched loops or junctions, to G-quadruplexes, a property

which is often explored in the development of biosensors[41, 43]. Compared to receptors with much larger sizes, the short aptamer can bring charged cytokine molecule more closer to the graphene surface upon binding to the target which could enhance the sensitivity of cytokine detection[22].

In the SELEX process, the aptamers are produced by repetitive cycles of washing and isolating the target-bound oligonucleotides and amplifying them until a high target-affinity oligonucleotide chain is created[44]. Aptamers that are specific to a certain cytokine is achieved by their unique sequence. In the present study, our focus was to develop an aptamer-based cytokine sensor to detect TNF-α. According to a study carried out by Orava W. E. et al., it has been identified that the aptamer sequence TGG TGG ATG GCG CAG TCG GCG ACA A, also known as the VR11 sequence shows the best specificity for TNF-α cytokine[45]. After a certain aptamer has been processed through several modifications in the SELEX process, it has ends known as the 3’ end and 5’ end. In order to immobilize the aptamer on the sensing area an anchoring group is employed. For the present study, aptamers with a modified 5’ end such that it contained either a thiol anchoring group or an amine anchoring group were used. Furthermore, the aptamers were modified such that it contained a fluorescence tag (FAM) at the 3’ end meaning that fluorescence spectroscopy can be used as a secondary verification of the presence of aptamers on the sensing area.

Chapter 3. Synthesis & Characterization Methods

2-D materials such as TMDs can be obtained in two ways, known as the top-down or bottom-up methods [46]. In the top-down method, the process of thinning down the nano-sheet from the bulk material is carried out via physical or chemical methods such as mechanical exfoliation, chemical exfoliation, or solution-based exfoliation. In the Bottom-up method, nanoscale materials are constructed from the atomic or molecular precursors such as via a CVD process [46].

There were two types of TMD materials that were employed for this project: WS_2 and MoS_2. The WS_2 crystals were synthesized using a CVD process whereas the MoS_2 crystals were obtained using mechanical exfoliation.

3.1. Chemical Vapor Deposition (CVD)

CVD is a widely used synthesis process to produce high-purity materials including TMDs such as WS_2, and MoS_2 etc. TMD CVD synthesis processes can be classified into three categories based on the growth technique [47-49]. They are vaporization and decomposition of metal oxide, vaporization and decomposition of chalcogen precursors, deposition of TMD on a substrate.

To synthesize the WS_2 crystals needed for this project, a process carried out by Lee Yi. H. et al. to synthesize MoS_2 employing the vaporization and decomposition of metal oxide was extended for WS_2 [47]. The initial trial and error process in order to optimize the growth parameters to obtain WS_2 crystals, were carried out by a former graduate student, Bakhtiar Azim. Once he was able to successfully optimize the CVD process, we were able to incorporate the same parameters to obtain the required WS_2 crystals on SiO_2 substrate for biosensing applications. During the synthesis of the TMD via metal oxide sulfurization, the metal oxide precursor undergo a two-step reaction in the gas phase. First, transition metal sub-oxides likely form and then the sulfurization of the sub-oxide leads to the formation of the TMD.

The required precursors for the CVD process, WO_3 (>99.5% purity) and S (>99.5% purity) were purchased from Sigma Aldrich. The SiO_2 (300 nm)/Si wafers were bought from Wafer Pro (Diameter: 100 mm, Orientation: <100>, Single Side Polished). The

Si/SiO_2 substrates were cleaved into 1 cm x 1.5 cm substrates. The cleaved substrates were then cleaned with acetone, IPA and Deionized water (DI water) and dried with nitrogen (N_2).

The WO_3 and S precursors along with the Si/SiO_2 substrates were placed in a 30 cm long quartz tube with a diameter of 6 cm. The quartz tube had one end opened and the other end closed. To facilitate the face down growth approach, we have used two cleaved and cleaned Si/SiO_2 substrates where one with WO_3 sprinkled on was used as the bottom and other face down, on top of the bottom, as the growth- substrate. The two sandwiched Si/SiO_2 substrates were then placed inside the closed end of the quartz tube. Figure 2 shows the placement of the WO_3 seeds and the Si/SiO_2 substrate (3 cm x 4 cm) serving as the S boat which was placed at the open end of the quartz tube. Figure 3 illustrates the optical images of the placement of growth substrates and the S boat.

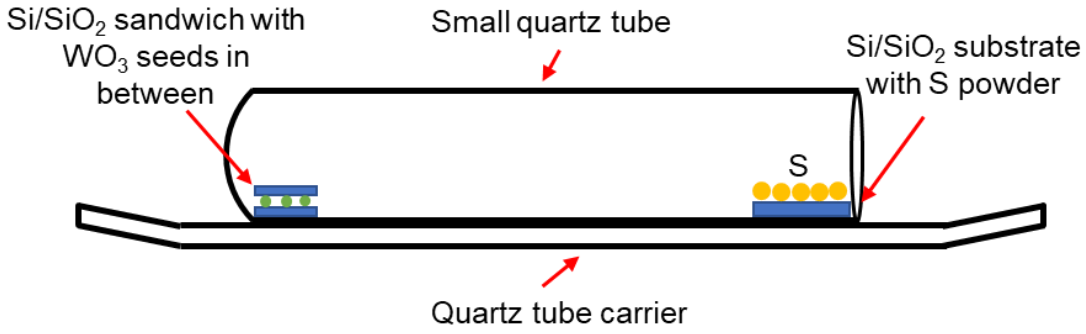

Figure 2: Schematic of the CVD reactor (not to scale).

For the synthesis of WS_2, we have used a small amount of WO_3 (which was sprinkled on the small bottom Si/SiO_2 substrate) and of S powder (1 g placed on the S boat). Once the sources were placed inside the small quartz tube the tube was inserted into the furnace using a carrier so that the open end was facing the gas inlet.

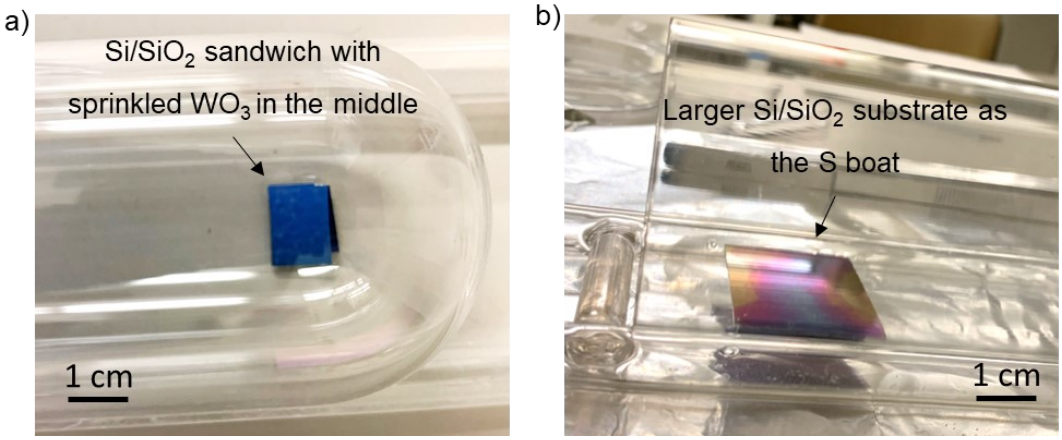

Figure 3: Photograph of a) Placement of the Si/SiO_2 substrates at the end of the quartz tube b) Placement of the larger Si/SiO_2 as the S boat.

A furnace with 3 heating zones was used as shown in the diagram in Figure 4. The quartz tube was placed 42 cm from the oven entrance so that the sandwiched Si/SiO_2 substrates with WO_3 was placed in zone 3 and the S source was placed in zone 2. Argon (Ar) gas (2 SCFH flow rate) was allowed to flow into the furnace acting as the carrier gas to transport the S vapor towards the growth substrates and facilitate the formation of WS_2 crystals. Once the furnace cap was tightly sealed (at the exhaust side) and the gas outlet was properly connected to the exhaust, the temperature in zone 3 was set to increase up to 800 ^{0}C which would bring the temperature of zone 2 to 180 ^{0}C. Therefore, during the synthesis of the WS_2 crystals, the growth substrate and the S source were kept at 800 ^{0}C and 180 ^{0}C respectively. Once zone 3 reaches 800 ^{0}C, the system was left for 30 min to react. After 30 mins the temperature in zone 3 was reset to room temperature and allowed to cool. Once the surface cooled to below 100 ^{0}C, the Ar flow was switched to N_2 flow and the quartz tube was taken out of the furnace.

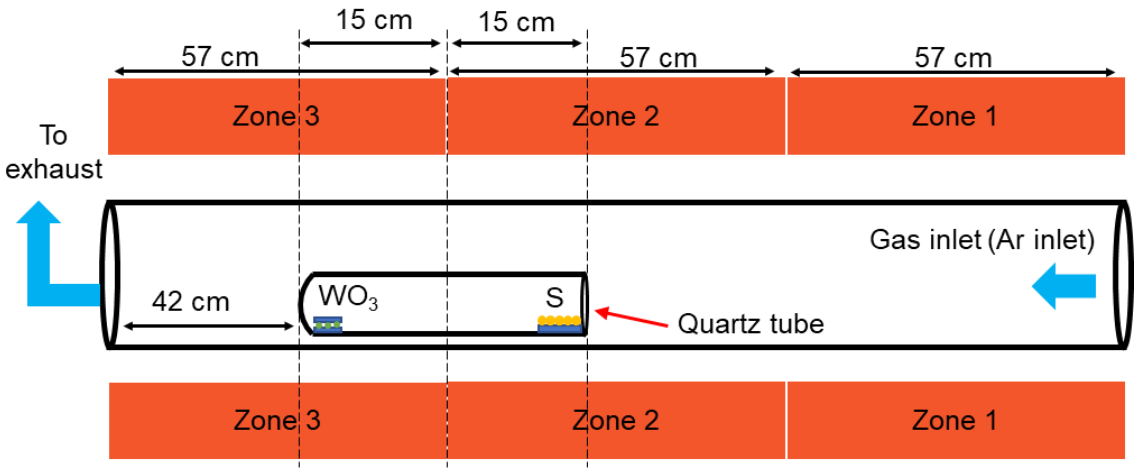

Figure 4: Schematic of the interior zones of the CVD reactor (not to scale).

Once the quartz tube was taken out of the furnace, the Si/SiO_2 substrates at the closed end of the tube were taken out carefully and were checked under the microscope. Optical images obtained for mono layer and multilayer WS_2 crystals synthesized via this CVD process are shown below in Figure 5a) and b).

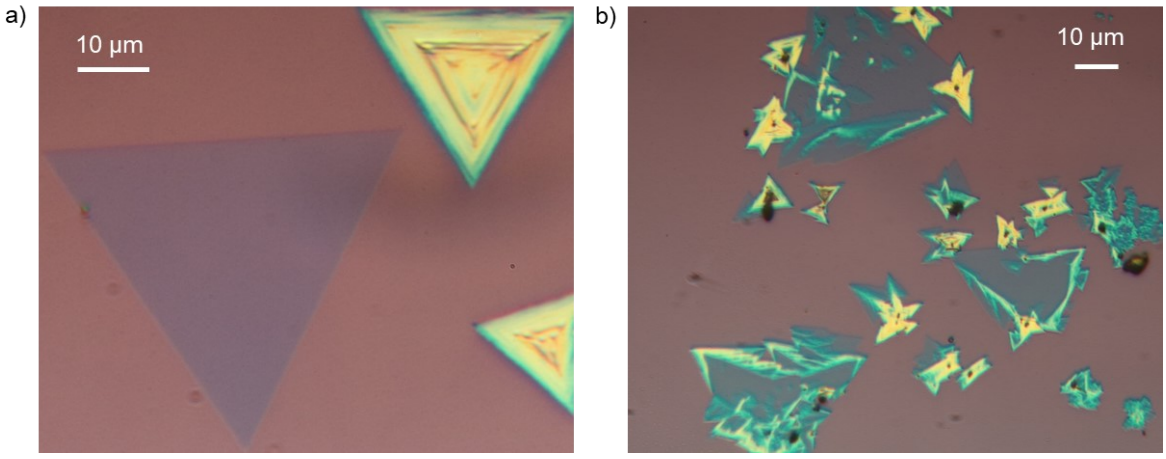

Figure 5: Optical images of CVD grown WS_2 crystals a) Large monolayer b) Nonuniform crystals.

3.2. Mechanical Exfoliation

As mentioned earlier, the MoS_2 flakes for the biosensor were obtained via mechanical exfoliation. Mechanical exfoliation is a method to obtain few layer or even one layer nanosheets [46]. In fact, graphene was first exfoliated using this technique which involves peeling off layers of carbon atoms from graphite using

an adhesive tape, a technique which has been extended for many 2-D materials [50]. This method yields high quality layers free from dopants that might be introduced from chemical processes. However, the disadvantages of this method are its improbable industrial scaling and limited crystal sizes. Nevertheless, mechanical exfoliation remains the most efficient way to produce the cleanest, crystalline and atomically thin nanosheets of layered materials such as MoS_2 [51].

In order to exfoliate the MoS_2 flakes, we have used cleaned Si/SiO_2 (Diameter: 100 mm, Orientation: <100>, Single Side Polished) as the substrate, which were cleaved into 1.5 cm X 1.5 cm pieces. Then thin MoS_2 crystals were first peeled from the bulk crystal using Scotch tape. These freshly cleaved MoS_2 flakes on tape were brought in contact with the clean Si/SiO_2 and rubbed using a Q-tip [51]. After removing the Scotch tape, the substrates containing the flakes were cleaned with acetone, IPA and DI water and observed under the optical microscope. Figure 6 a) and b) illustrates optical microscopic images of exfoliated few layer MoS_2 crystals.

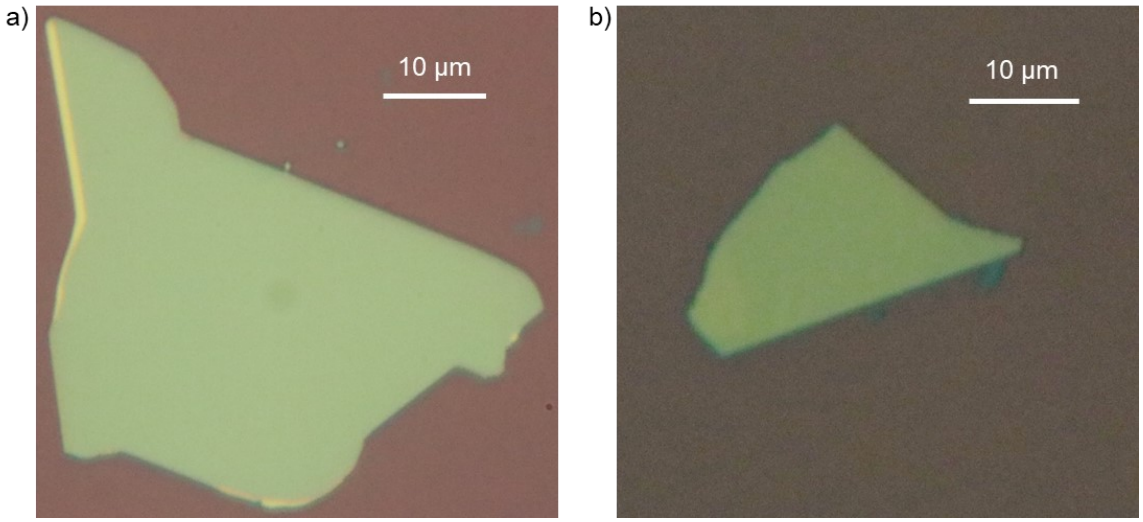

Figure 6: a) & b) Exfoliated MoS_2 flakes.

3.3. Atomic Force Microscopy (AFM)

Measuring the thicknesses of ultra thin films or flakes with accuracy is a challenging task. AFM is a very high-resolution scanning probe microscopy with resolutions capable of fractions of a nanometer [52]. In AFM imaging, a sharp cantilever tip is incorporated to “feel” the surface and thus gives a map of topology of the sample

surface. Apart from thickness profiles, AFM can also extract information on the roughness or material characteristics[53].

AFM follows a working principle based on changes in attraction and repulsion forces between material and tip, caused by van der Waals interactions. The probing is conducted by a tip (with a radius of curvature on the order of few nanometers) which is mounted to the end of a cantilever[54]. The cantilever allows the tip to be moved up and down as it scans the sample. Since the cantilever has a very low spring constant, it allows the AFM to control the force to a great precision[54].

In this project, the AFM measurements were incorporated to obtain the thickness profiles of the flakes using the tapping mode. In the tapping mode, the cantilever is made to oscillate and the tip "taps" across the surface, giving information of the surface topology [55]. During the measurement, the surface of the sample placed on a piezoelectric holder is being scanned by the tip. Any change in the force between the tip and the sample leads to a deflection in the cantilever. This deflection is detected using a laser source and a photodetector. This data is then fed to feedback electronics and is processed into images. These images are then analyzed using a specific software to obtain the height profile of the image[54]. The AFM imaging to extract the thickness profiles were obtained using an Asylum (MFP3D) AFM (show in Figure 22 under Experiments, Results and Discussion).

3.4. Kelvin Probe Force Microscopy (KPFM)

KPFM is another type of a measurement that can be carried out using an AFM apparatus. KPFM allows the measurement of the local contact potential difference (CPD) between a conducting AFM tip and the sample, which will map the work function or surface potential of the sample with high spatial resolution [56]. The CPD (V_{CPD}) between the tip and the sample is defined as

$$V_{CPD} = \frac{\Phi tip - \Phi sample}{-e}$$

Where Φtip and $\Phi sample$ are the work functions of the tip and the sample and e is the electronic charge. When an AFM tip is brought close to the sample surface, an electric force is generated between the tip and sample surface caused by the difference in their Fermi energy levels. Equilibrium requires Fermi levels to line-up at steady state, if the tip

and sample surface are close enough for electron tunneling. Upon electrical contact, the Fermi levels will align through electron current flow, and the system will reach an equilibrium state. The tip and sample surface will be charged, and an apparent V_{CPD} will form [56]. It is important to prepare atomically sharp and conducting AFM tip for high resolution KPFM.

KPFM has high spatial resolution with relatively high energy sensitivity, but it does have some disadvantages. One of the main disadvantages is that, an abrupt topographic height change can disrupt the accurate measurement of KPFM [56]. This causes many issues when trying to obtain a KPFM image for devices contacts often contain rough edges which affects the KPFM measurements.

3.5. Fluorescence Spectroscopy

Luminescence is the emission of light from any substance and occurs from electronically excited states divided into two categories phosphorescence and fluorescence[57]. Phosphorescence is a radiational transition, in which the absorbed energy undergoes intersystem crossing into a state with a different spin multiplicity. The lifetime of phosphorescence is usually longer than fluorescence. Fluorescence in a biological sample is a photosynthetic reaction. Typically, fluorescence can be excited by a light source with a peak emission in the ultraviolet (UV) (or even violet in some cases) range with the fluorescence emission peak occuring at a longer wavelength. Figure 7 shows an illustration of the energy transfer between the energy levels during a fluorescence emission.

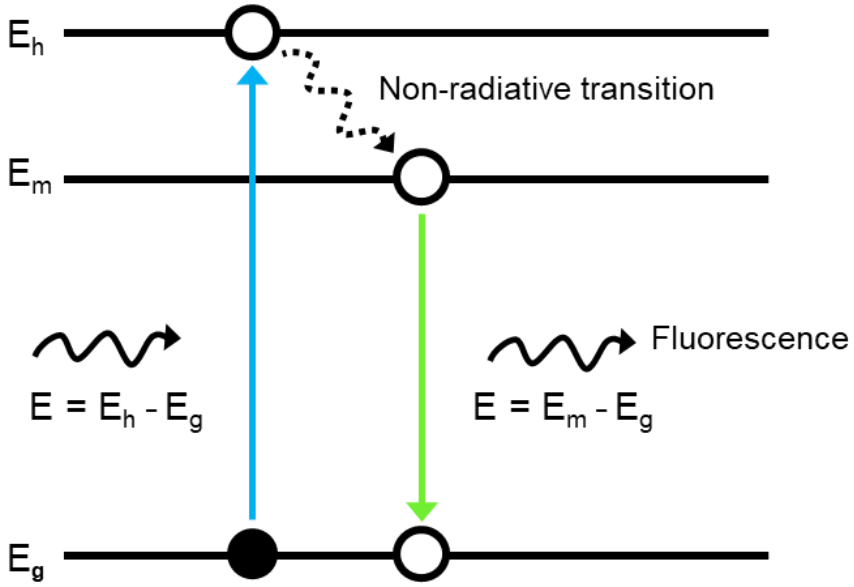

Figure 7: Energy transfer during fluorescence emission.

During excitation, an electron in the ground state (E_g) absorbs a photon and acquires a higher energy (E_h). Electrons in higher exited states are highly unstable hence it instantly releases some of the energy to the surroundings (e.g. as heat) and undergoes a non-radiative transition to a meta-stable state (E_m). A metastable state may have a longer lifetime and a lower energy compared to E_h, the electron's lifetime in the metastable state is still only about several nanoseconds. The electron re-emits the remaining energy as fluorescence and returns back to its ground state E_g.

Generally, fluorescence data are presented as an emission spectra. A fluorescence emission spectrum is a plot of the fluorescence intensity versus wavelength or wavenumber[57]. The aptamer receptors employed in this project contain a fluorescence tag (FAM) which emits a fluorescence peak at 525 nm wavelength once excited by an UV source. Therefore, fluorescence spectroscopy has been used as a secondary verification method to confirm the presence of the aptamers on the sensing area.

3.6. Probe Station for Electrical Measurements

In order to investigate the biosensors performance, the devices were tested with current-voltage (I-V) measurements. Electrical measurements were performed using a

semiconductor characterization system (Keithley 4200-SCS) connected to a probe station at room temperature. As explained in Chapter 2, a FET typically consists of three main terminals, known as gate, drain and source. For initial measurement of the intended FET cytokine sensor, only the current cross the source and drain through the sensing material (either WS_2 or MoS_2) was measured. However, after encountering few challenges the device design was changed to a diode sensor which only required a two-probe measurement across the sensing material.

I-V measurements typically involve the use of several instruments, ammeter, multiple voltage sources and voltmeters. Semiconductor characterization system programs synchronize multiple source measurement units (SMU) to quickly and accurately source and measure both current and voltage. The system can achieve a low current resolution (up to 0.1 fA) and can be current limited (using the compliance option) to prevent damage to the device [58]. Using this system, we were able to simultaneously sweep the voltage within a certain voltage window with a specific voltage step size and to also measure the current response.

Since the fabricated devices were micron in scale, the I-V characterization system were connected to a probe's station where contacts were made with probes using a microscope. Figure 7 illustrates an optical image of the probe station setup where two probes used for the I-V measurements are shown to be connected to the device and a third probe can be seen at the back of the system. The whole system has a robust enclosure to minimize interruptions from the background light and vibrations. Also, in order to eliminate any current leakage through the chuck, the devices were placed on a plastic stage during measurement.

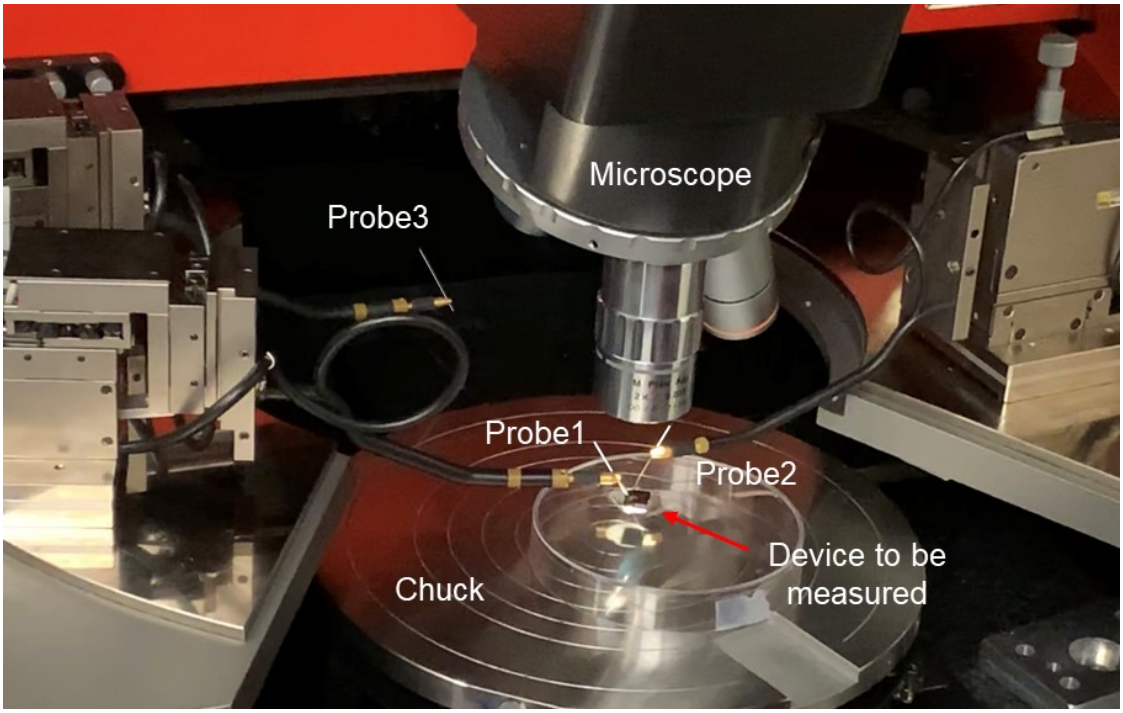

Figure 8: Probe station setup.

Chapter 4. Experiments, Results and Discussion

In this project, two separate approaches were considered for the development of the aptamer-based cytokine sensor. The initial attempts at developing the sensor involved a FET-based design employing thiol terminated aptamers. The second approach was based on a novel design incorporating amine-terminated aptamers, which will be discussed later in the chapter.

4.1. FET-based cytokine sensor employing thiol-terminated aptamers.

4.1.1. Device fabrication methods.

Since the thiol-terminated aptamer immobilization is highly favored by the existence of S vacancies, CVD grown WS_2 (employing the process mentioned in the previous chapter) flakes which are enriched with S vacancies[59] were chosen as opposed to the exfoliated flakes. A schematic of the fabrication steps is shown in the Figure 9.

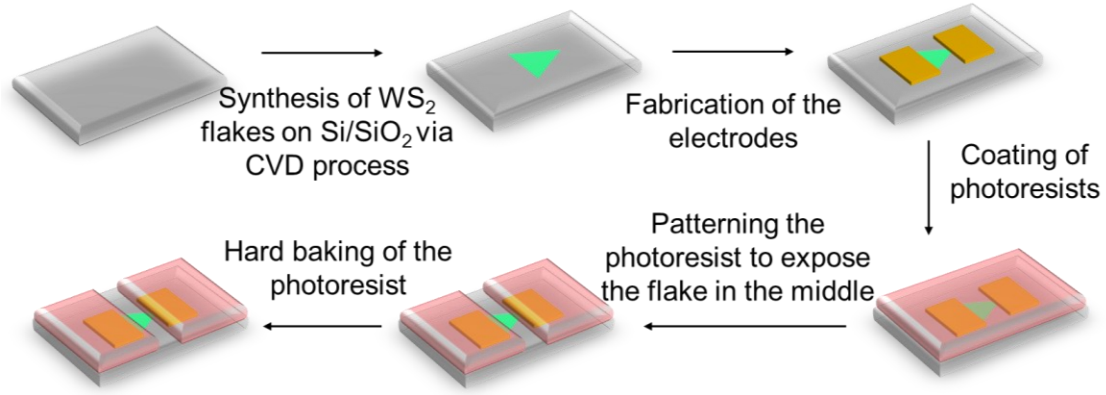

Figure 9: Fabrication process with positive photoresist as the passivation layer.

WS_2 flakes were synthesised via the CVD process mentioned in the previous chapter. For electrical contacts, electrodes were patterned via photolithography. Cr (10 nm) and Au (50 nm) layers were deposited on to electrodes by thermal evaporation following photolithography. For the surface of surface passivation positive photoresist (Microposit S1813) was spin coated over the sensor. The purpose of the surface passivation layer is to provide an insulation against any liquid introduced during the

measurements. A thin stripe over the WS_2 sensing area and the electrode pads cleared of photoresist using photolithography. The remaining photoresist layer was hard baked (110 ^{0}C for 10 min). During measurements, the cytokines were introduced in a phosphate-buffered silane (PBS) solution purchased from Lonza. It was imperative to avoid contacting the metal electrodes with the PBS to avoid leakage current. A special electrode design as shown in Figure 10 a) was implemented with longer arms to the contact pads, placed far away from the sensing area. With long electrode arms (which can be easily coated with photoresist) the probes can connect to the sensor without being in contact with the PBS in the sensing area. A schematic of a cross section of the sensing area (with the passivation photoresist layer) is shown in Figure 10 b).

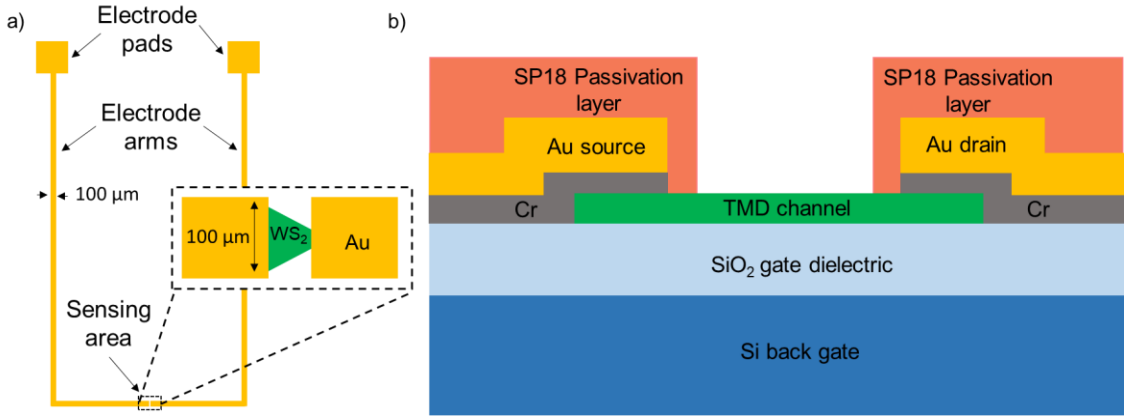

Figure 10: Cytokine sensor design a) Top view showing electrodes with longer arms b) Cross section of the sensing area.

After the passivation step and before further processing, the device was tested in PBS to verify the effectiveness of the passivation layer by measuring the I-V response in the voltage window of -3 V to 3 V. The passivation layer should provide electrical isolation to the Au electrodes during measurement in PBS hence ensure the device stability. Figure 11 shows an optical image of the device connected to the probes for measurements.

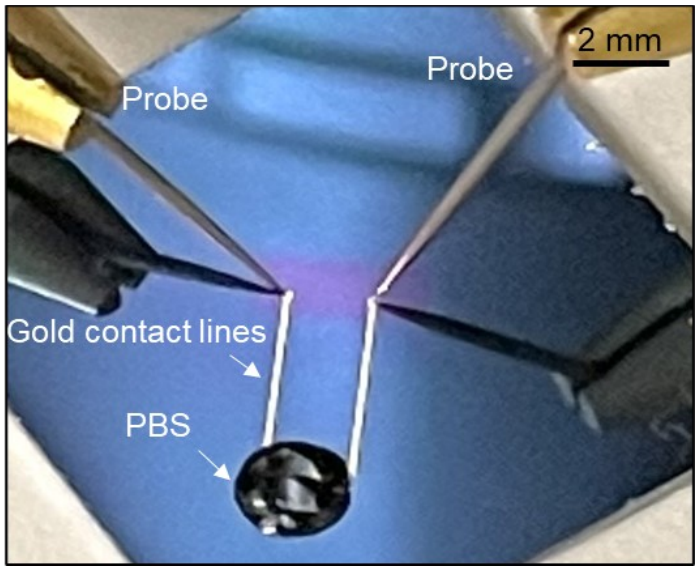

Figure 11: Photograph of the probe station setup with the device attached to the probes.

Figure 12 shows optical images of the sensing area before and after I-V measurement. In Figure 12 a), the passivation photoresist is coated everywhere except in the middle stripe so that the WS_2 flake area in the stripe will be exposed to the PBS drop casted during the measurement.

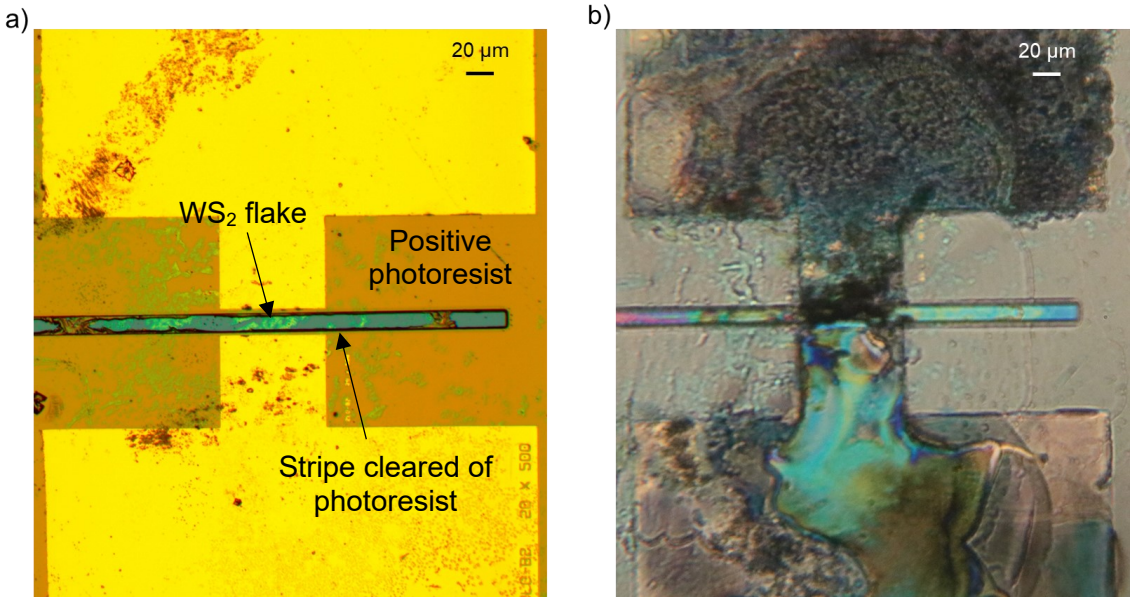

Figure 12: Photograph of the sensor with photoresist passivation a) Before and b) After I-V measurement.

However, as shown in Figure 12 b) during the measurement, the flake and the area around the flake changed colour. A clear discolouring, and degradation of the electrodes around the sensing area confirms the failure of the S1813 photoresist passivation layer.

After observing the inability of the S1813 photoresist to be used as a passivation layer, an alternative material was needed. In the second design, SU-8 negative photoresist, which has displayed adequate passivation properties [60], was employed as the passivation layer. For example, a previous study based on a graphene FET sensor for the detection of covid has incorporated SU-8 photoresist as the surface passivation layer to minimize the current leakage [60]. In this study, we have incorporated SU-8 2005 photoresist with a thickness 5 µm. The fabrication process for the sensor with the SU-8 passivation layer is shown in Figure 13.

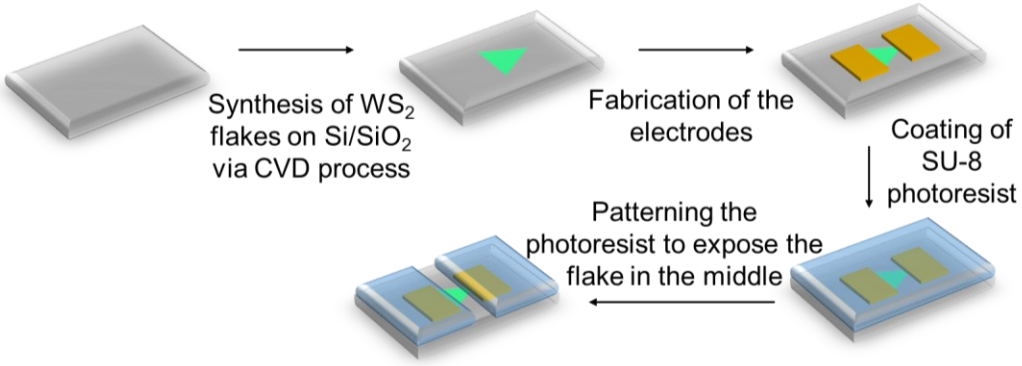

Figure 13: Process steps with SU-8 passivation layer.

The fabrication process with the SU-8 passivation layer is almost identical to the process with the positive photoresist passivation layer except that during the post-exposure bake, the SU-8 layer was baked at 95 ^{0}C for 3 min. Figure 14 shows optical micrographs of the SU-8 passivation around the sensing area, with the stripe in the middle over the WS_2 flakes. After SU-8 passivation, the initial devices were tested with a PBS droplet introduced in the sensing area to verify the effectiveness of the passivation layer by measuring the I-V response in the voltage window of -3 V to 3 V.

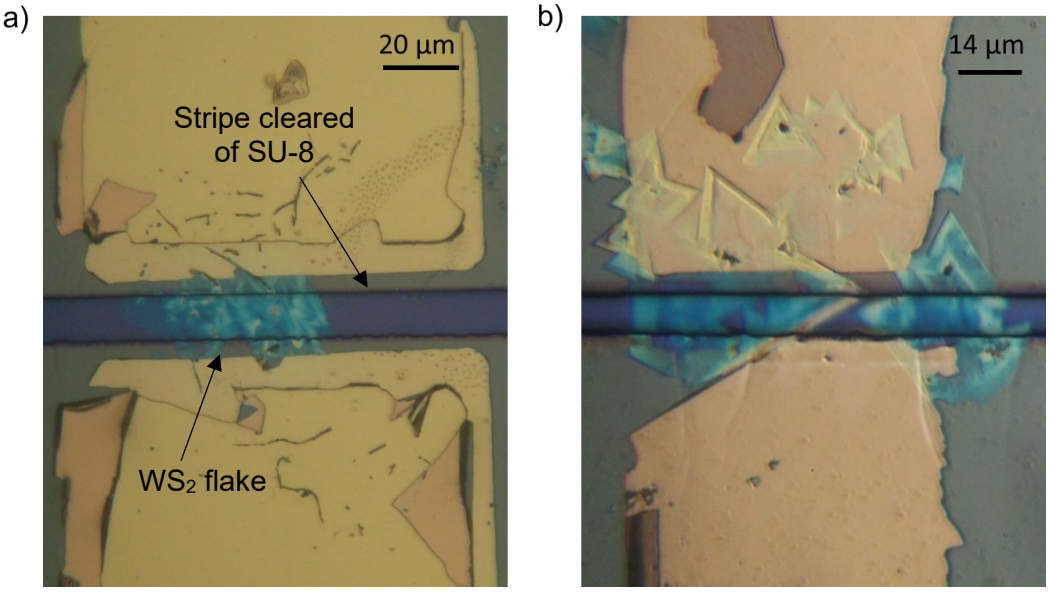

Figure 14: Photograph of the sensing area with SU-8 passivation a) Device 1 (D1) b) Device 2 (D2).

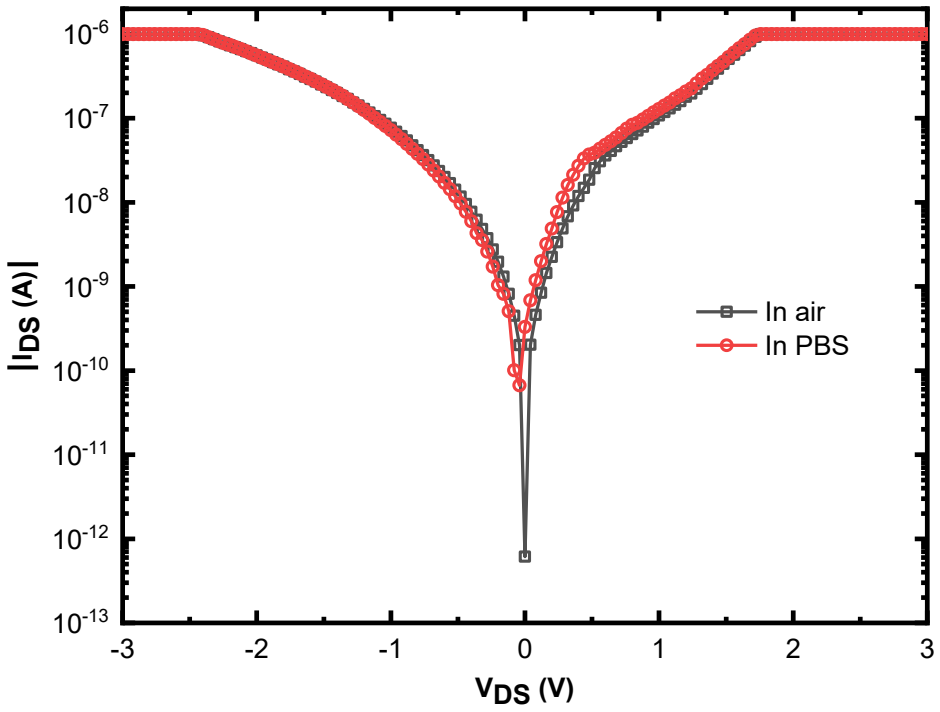

Figure 15: I-V response for D1 with SU-8 passivation in air and in PBS.

Figure 15 illustrates the I-V curve obtained for device 1 (D1) with SU-8 passivation measured in air and in PBS, where the current was measured across the flake (I_{DS}) while the voltage across the flake (V_{DS}) was swept from -3 V to 3 V. During the measurement, the gate voltage was left floating. All I-V measurements were conducted with a scan speed

of 40 mVs^{-1}. Since the I-V response of D1 in air and in PBS shows a similar response, the SU-8 photoresist showed promising results to be used as a passivation layer. Furthermore, no change in colour was observed during measurements.

After observing good passivation behavior for device D1, it was functionalized with thiol ended aptamer linkers. The thiol terminated aptamer sequence, /5ThioMC6-D/TCC ATG ACG TTC CTG ACG TT was synthesized and purified by Integrated DNA Technologies (Coralville, USA). The as-received thiol aptamer sample was reconstituted in IDTE buffer (10 mM Tris, 0.1 mM EDTA) purchased from Integrated Technologies (100 μM) and aliquoted into volume for storage at -20 ^{0}C. In order to prepare the aptamer sample for the functionalization, a 100 μL from 100 μM aptamer sample was diluted in 900 μM IDTE buffer to obtain a 1 ml of 10 μM aptamer solution. To facilitate the aptamer immobilization on the WS_2 flakes, the device D1 was dipped in the diluted 10 μM aptamer sample prepared, for 1 day. After 1 day, the sample was taken out of the aptamer solution, washed thoroughly in Molecular biology grade water (N-free water) purchased from Lonza in order to remove the physiosorbed aptamers and stored at -20 ^{0}C until measurement.

Figure 16 compares the current across the WS_2 flake while the voltage was swept from -3 V to 3 V, before and after aptamer coupling. The gray curve is the I-V response in PBS for the pristine flake (before aptamer functionalization). The red curve is the first measurement of the I-V response in PBS after aptamer functionalization. When compared there is a significant decrease in the current level. During thiol terminated aptamer coupling, the S atom in the thiol anchoring group is expected to covalently bonds with the vacancy sites on the WS_2 surface, hence passivating the vacancies. Therefore, following the thiol functionalization process, a decrease in the surface current is expected and observed [35]. However, during the immediate repeat of the I-V measurement (After M2) the current increased back to the pristine state as shown by the blue curve. One possibility for this observation could be due to a weak coupling of thiol anchoring groups at the vacancy sites.

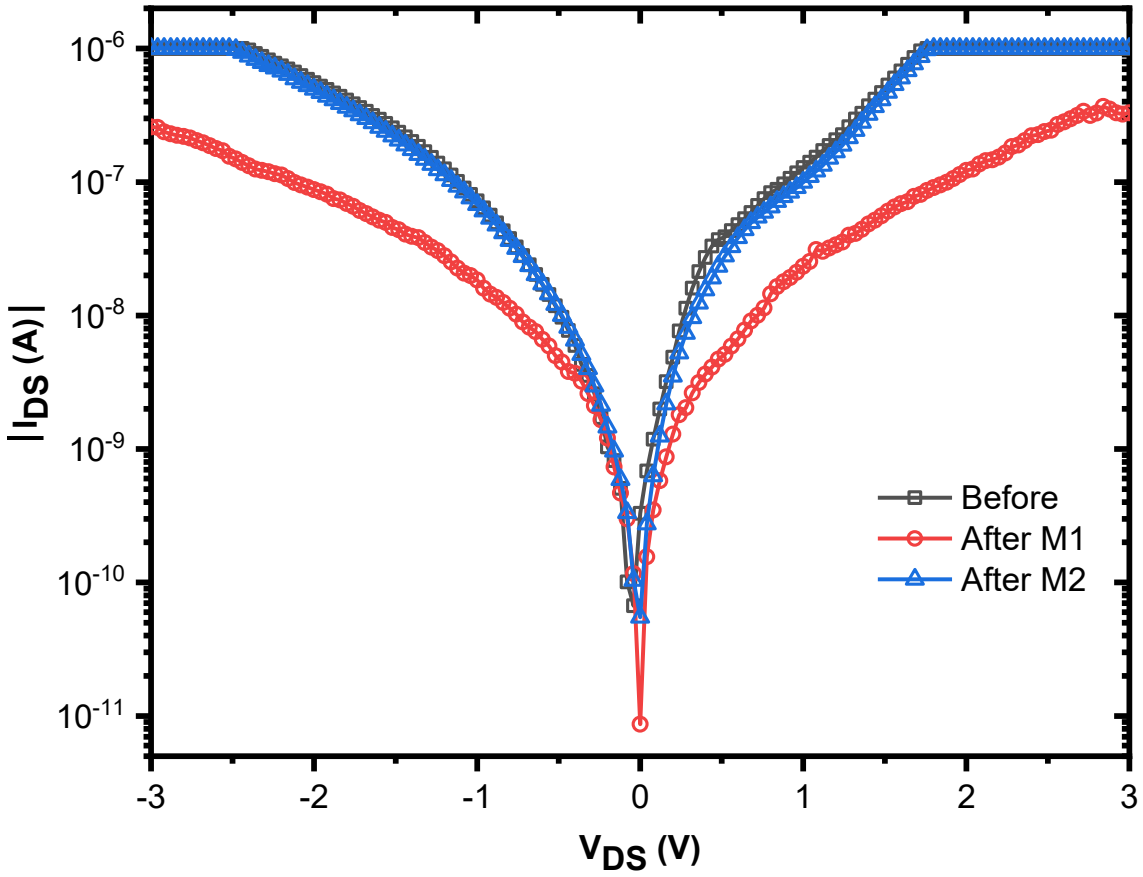

Figure 16: I-V measurement for D1 before and after aptamer functionalization.

In order to further investigate the observation seen above, several attempts were made to test more devices (D2 and D3). However, during the preliminary measurements in PBS, these devices oxidized similarly to the initial devices passivated with the S1813 photoresist, where a discoloring and destruction of the electrodes around the sensing area was observed. Figure 17 shows the optical micrographs of discoloured devices.

One of the interesting observations seen in the devices in Figure 17 is that the possible oxidized areas on the devices are mostly limited to the exposed area of the WS_2 flake, the boundary of SU-8 passivation layer along the opening of the sensing area and the electrode area closer to the SU-8 boundary. During the spin coating of SU-8 photoresist, it was observed that the surface areas with high WS_2 flake population displayed hydrophobicity, which discouraged the fine adhesion between SU-8 and the surface. Due to this nature of the spin coating, it is possible that the SU-8 did not get completely coated near the WS_2 flakes, which caused the flake area and the electrode

near by to get oxidized during measurement in PBS. In fact, the only device that showed adequate SU-8 passivation was D1.

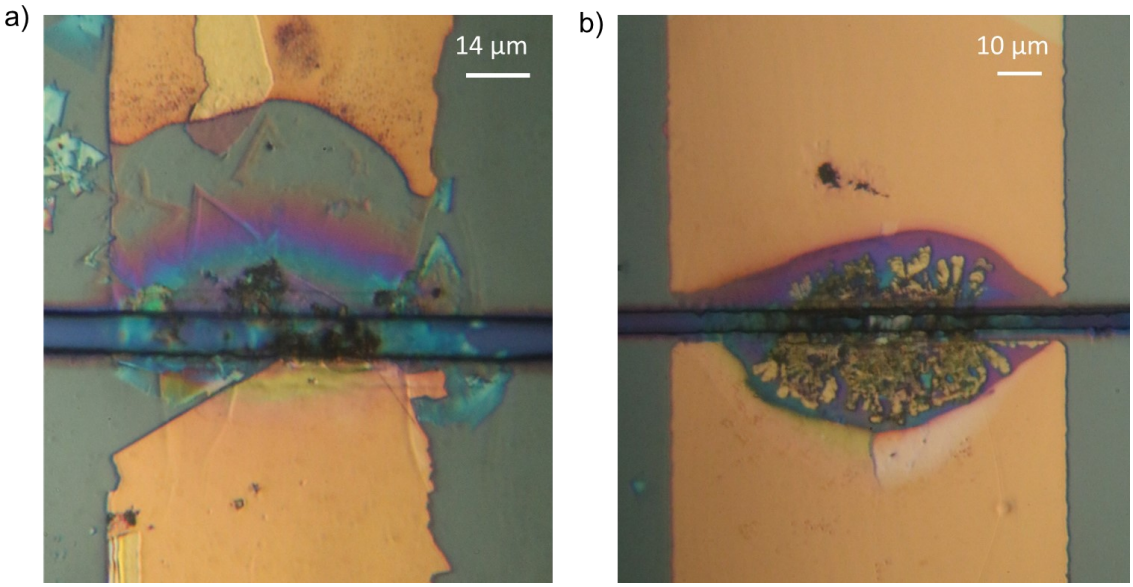

Figure 17: Discolouring of the sensor after measurements in PBS a) Device 2 (D2) b) Device 3 (D3).

Since the failure of SU-8 photoresist as a passivation layer, in the third fabrication design, Al_2O_3 was incorporated for surface passivation purposes. The Al_2O_3 was deposited using the atomic layer deposition (ALD) technique. ALD is a technique widely popular in nanodevice fabrication since it allows thickness control at the atomic level [61]. Apart from this, ALD can deposit very conformal and ultrathin films on substrates with very high aspect ratios [61].

Figure 18 illustrates the fabrication process of the initial device structure with an Al_2O_3 passivation layer. After synthesis of the WS_2 crystals on the Si/SiO_2 substrate and depositing the electrodes, a Al_2O_3 layer (70 nm) was deposited using the ALD (Cambridge Nano Tech Fojo F200) system. During the formation of AL_2O_3 layer, the starting surface is exposed to a metal organic precursor such as Trimethylaluminum (TMA) that reacts with the surface in a self-limiting reaction[62]. Once the system is purged with an inert gas to remove excess precursors and by-products, a second co-reactant is introduced and reacts to form one monolayer of Al_2O_3 ALD[62]. By repeating this cycle, more Al_2O_3 layers can be grown. After the deposition of the Al_2O_3, the flake in the middle was exposed by etching a narrow stripe over the flake using buffered oxide etchant (BOE).

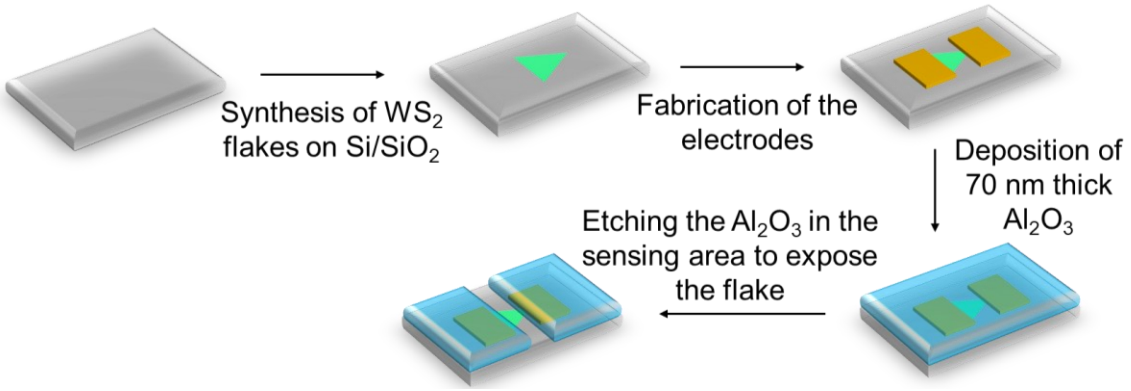

Figure 18: Process steps with Al_2O_3 passivation layer.

Figure 19 a) and b) shows the sensing area of the cytokine sensors with Al_2O_3 passivation. Once the devices were fabricated, they were initially tested by measuring the I-V response while the flake area was being exposed to PBS buffer. The devices were still in pristine condition without undergoing any functionalization. However, in order to obtain the I-V response, the devices needed to be connected to the probe station. Therefore, the Al_2O_3 layer covering the electrode pads needed to be removed by etching the devices in BOE. Figure 20 shows the rectangular area over the contact pads (in red broken lines) that was cleared of the insulating Al_2O_3 layer to facilitate low resistive contact paths.

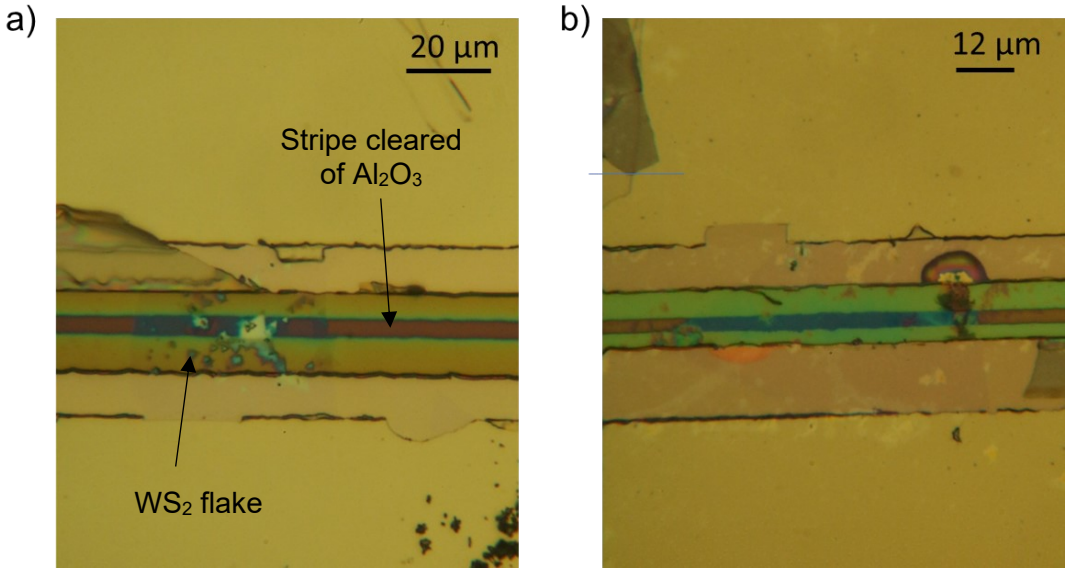

Figure 19: Sensing area showing the exposed WS_2 along the stripe cleared of Al_2O_3 passivation layer a) Device 5 (D5) b) Device 6 (D6).

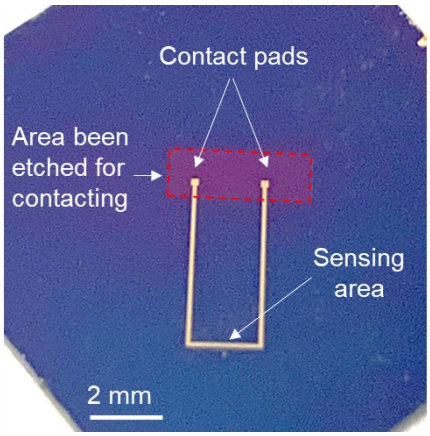

Figure 20: Photograph of the sensor showing the area cleared of Al_2O_3 passivation layer.

Figure 21 illustrates the I-V response obtained for D5 where the current was measured across the flake while the voltage was swept from -3 V to 3 V. The gray curve is the response in air and the red and blue curves were the subsequent measurements in PBS where M1 represents the first measurement and M2 represent the second measurement. Even though we did not observe flakes being oxidized during the measurements (which confirms the success of the Al_2O_3 passivation) subsequent measurements in PBS are varying. This is highly undesirable for a cytokine sensor since the initial baseline measurement in PBS needs to be stable for reliable cytokine detection. Apart from this, as a result of flake's direct contact with the PBS, the current level as increase compared to the measurement in air.

One reason for the instability in I-V measurements in PBS could be due to the flakes being directly exposed to PBS. This may cause a reaction to occur on the surface hence changing the I-V during repetitive measurements. It appears that the direct contact of WS_2 with PBS during a voltage sweep, increases the surface charges on the WS_2 layer, increasing the current levels. This is another undesirable effect to avoid. An alternative method was needed to immobilize the aptamer with a passivation layer over the flakes. As a result, more attention was given to the aptamer functionalization based on silane chemistry where TMD materials are often coated with an oxide layer such as SiO_2, Al_2O_3, or HfO_2 to facilitate the functionalization [39]. Incorporating a passivation layer over the TMD flakes on the sensing area would intuitively give it more stability during I-V measurements in PBS.

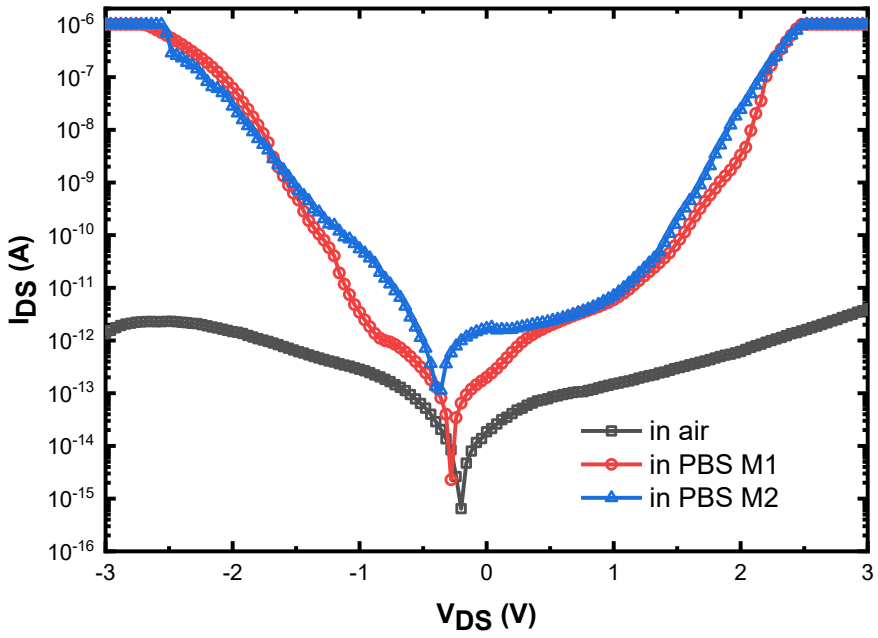

Figure 21: I-V measurements of D5 in air and in PBS.

4.2. Cytokine diode sensor based on amin-terminated aptamers.

For a device to be functionalized based on silane chemistry, a different approach was employed. A novel mechanism based on the rectification behavior observed for devices fabricated with asymmetric contact length/area TMD flakes. Compared to a FET based sensor, a diode sensor needs only two-probe measurements allowing us to avoid the gate current leakage issues. A diode sensor adheres to a much simpler design compared to a FET sensor.

4.2.1. Initial characterization and device fabrication methods.

For the fabrication of a cytokine diode sensor (CDS), MoS_2 flakes exfoliated from a bulk 2-H phase single crystal MoS_2 (ordered from 2D Semiconductors) were employed. Once the MoS_2 flakes were exfoliated onto a cleaned Si/SiO_2 substrate, the flakes were chosen such that their colour appeared to be a shade of blue or green under the optical microscope, with a shape closer to a triangle to maximize the asymmetry. Even though all the flakes used in this study appeared to be blue or green under the optical microscope, the thickness varied from flake to flake. Figure 22 shows the AFM thickness profile of

these flakes varied from 13 nm to 60 nm. The bluish and greenish (as appeared under the microscope) flakes had higher and lower MoS_2 thickness respectively.

Apart from the colour, attention was given to the shape of the flake since the rectification behavior of the MoS_2 diodes arises due to flake asymmetry, as reported for several other 2D materials[63-66]. Due to a change in the contact lengths and/or contact areas between the two electrodes, a considerable Schottky contact difference forms at the metal-semiconductor interface, giving rise to a diode behavior[64]. For example, Figure 23 shows about a one order of magnitude rectification observed for a triangular shaped a)ɛe which has shown in the inset of the graph. Apart from the irregular shape of the flakes, it is also possible to form a Schottky contact difference incorporating asymmetric electrodes with different work functions, and piezoelectricity[64]. However, in this work, we are only focusing on MoS_2 diodes fabricated based on the asymmetry of the flake itself.

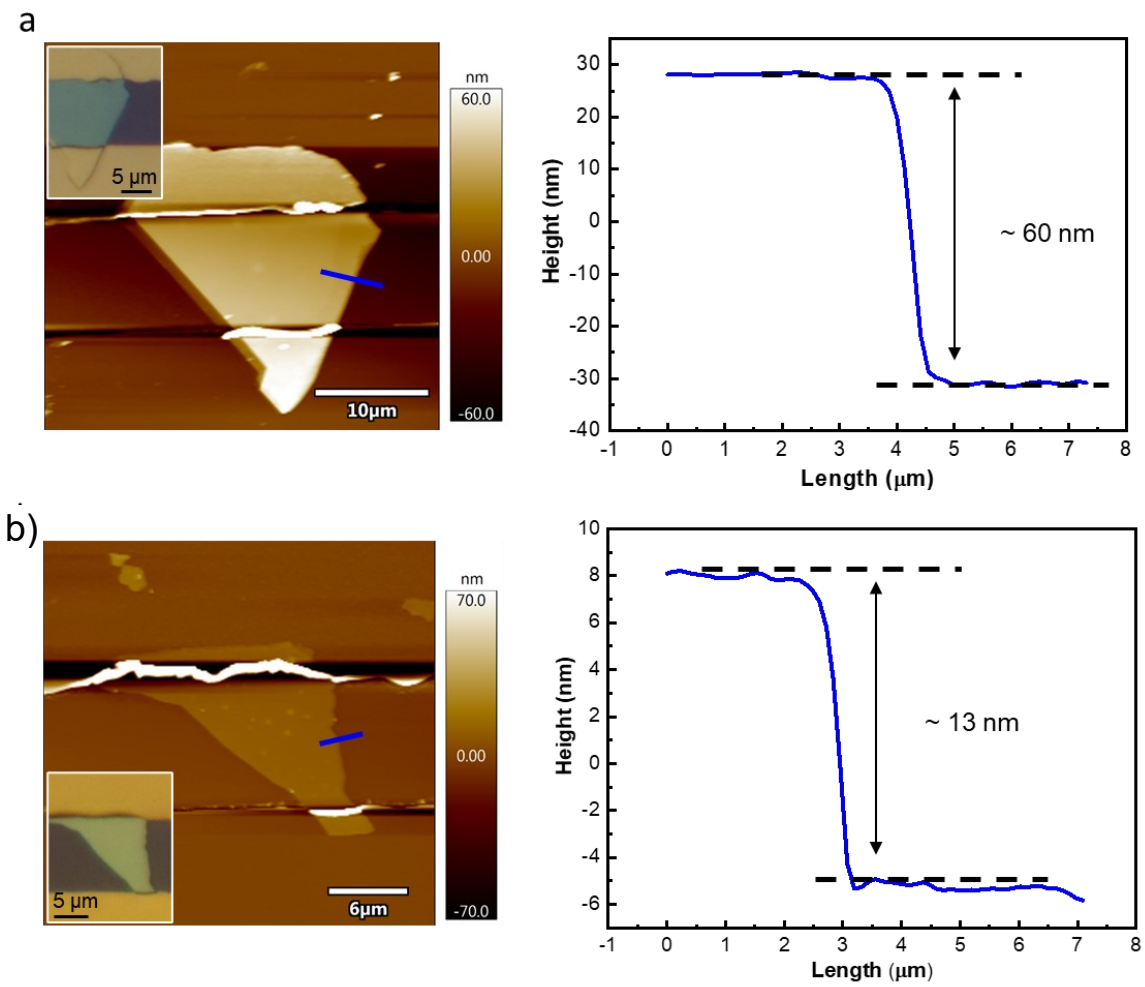

Figure 22: AFM measurement. Associate image and the height profile along the blue line in the image from 2 flakes. a) blue and b) green coloured optical images as shown in the insets.

During the I-V measurements in Figure 23 a), the shorter MoS_2/Au contact interface (right side contact pad shown in the inset) was grounded, and the longer MoS_2/Au contact interface (left side) was biased (V_{bias}) from -1 V to 1 V with a 0.04 V step size. For all the I-V measurements obtained for the diode sensor, the voltage source was connected in the same way (shorter interface grounded and longer interface to the voltage bias).

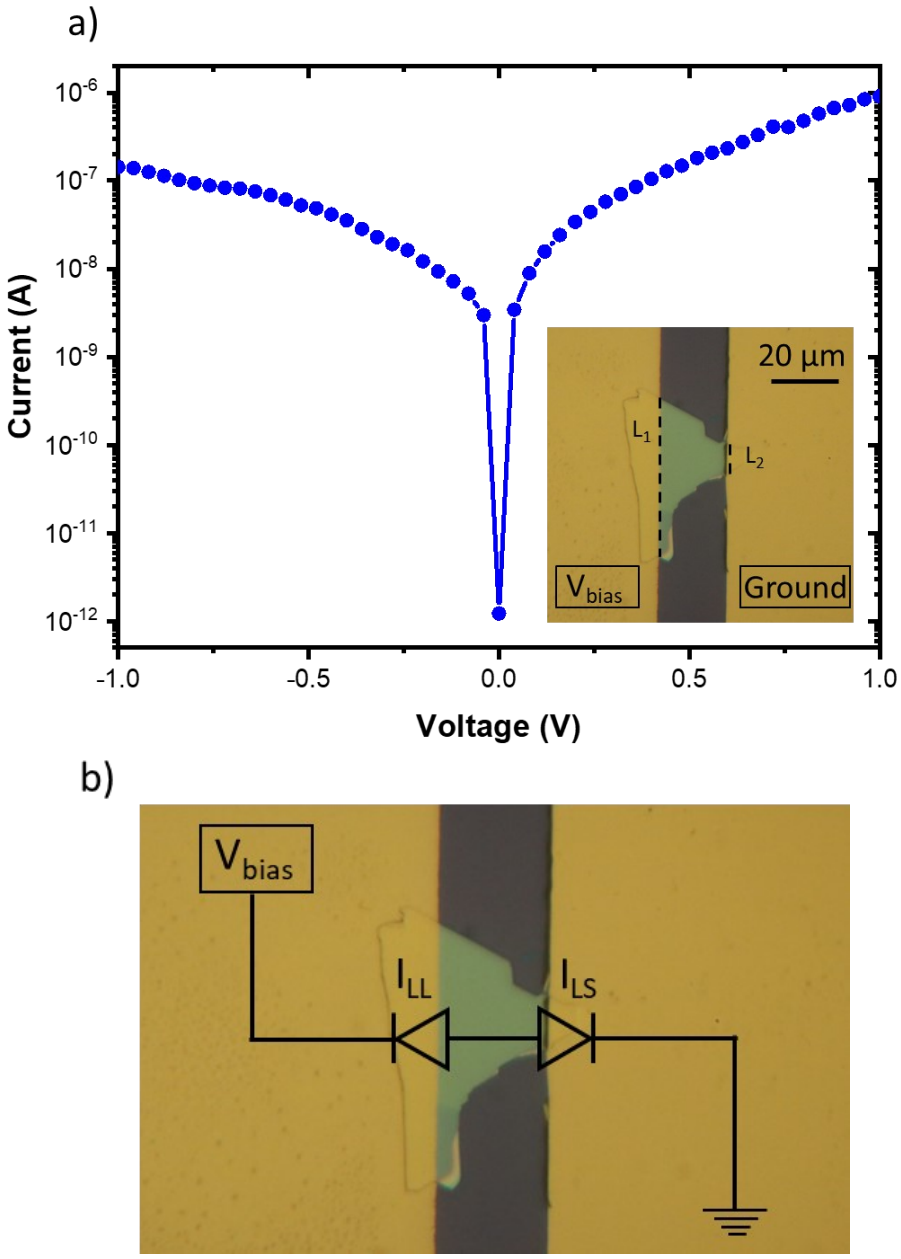

Figure 23: **a) I-V curve for asymmetric contact length/area flake showing diode behavior. An optical image of the flake is included in the inset b) schematic of the back-to-lback diode at the MoS_2/Au junction.**

Figure 23 b) shows the two MoS_2/Au contacts being connected like back-to-back diode circuit where the diode on the shorter interface ($DD_{shorter}$) is grounded while diode on the longer interface (DD_{longer}) is connected to the voltage source. At -1 V V_{bias}, DD_{longer} is forward biased and $DD_{shorter}$ is reverse biased. Therefore, the current at -1 V is due to the leakage current of $DD_{shorter}$, I_{LS}. At 1 V V_{bias}, $DD_{shorter}$ is forward biased and DD_{longer} is reverse biased. Therefore, the current at 1 V is due to the leakage current of DD_{longer}, I_{LL}.

We believe that due to the difference in the resistance at the two interfaces, where intuitively assuming the longer interface to have a lower resistance than the shorter interface (since resistance is proportional to the reciprocal of the area), $I_{LS} < I_{LL}$. Hence the current at -1 V is lower than the current level at 1 V, giving rise to the rectification behavior seen in Figure 23 a).

The following table contains how the rectification factor (Log |I at -1V| – log |I at 1V|) changes according to the degree of asymmetry of the device. The degree of asymmetry was calculated by taking the ratio between longer MoS_2/Au interface (L1 as shown in the inset of Figure 23 a) and the shorter MoS_2/Au interface (L2). The rectification factor is calculated by subtracting the log of the absolute current at 1 V from the log of the absolute current at -1 V.

Table 2: Rectification factor based on the degree of asymmetry.

Ratio between the lengths (longer length / shorter length)	**Initial rectification factor (Log |I at -1V| – log |I at 1V|)**
2.6	-2.69
2.6	-2.22
2.1	-2.3
1.71	-1.28
1.7	-1.65
1.64	-0.95

Table 2 has shown some evidence that the intrinsic rectification factor of the MoS_2 diode increases with the degree of asymmetry. A similar relationship between the rectification factor to the degree of asymmetry has been reported by G. Dushaq et al. for germanium arsenide (GeAs) where with the increase of GeAs/Au contact length asymmetry, the rectification factor increased. Figure 24 shows the plot of length ratio versus rectification factor for the MoS_2 diode sensor. As the asymmetry is increased (which is attributed to the ratio between lengths) the intrinsic rectification factor is increased. We believe that more data is needed to infer a trend between the intrinsic rectification factor and the length ratio. Nevertheless, it is evident that there is a strong relationship between the two parameters where the rectification factor is increased with the increasing asymmetry.

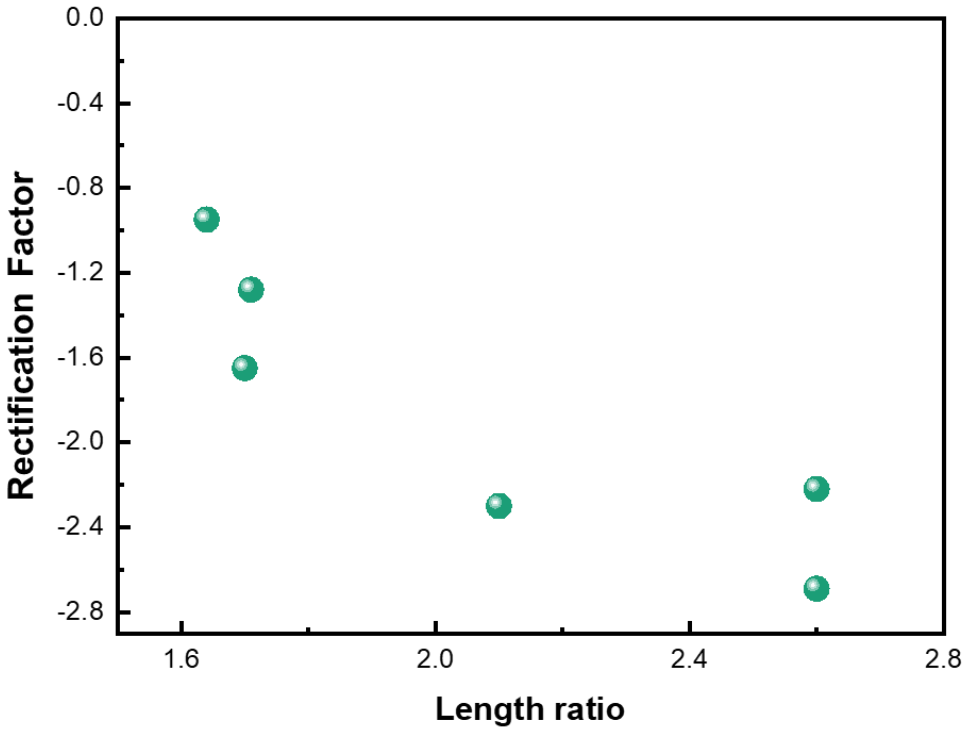

Figure 24: Plot of length ratio versus rectification factor

A complete understanding of the mechanism for the origin of the observation of rectification behaviour due to flake contact asymmetry has not been presented. One explanation involves Fermi level pinning. Fermi level pinning results from interface states that are formed at the interface between a metal and a semiconductor [67]. The Fermi level becomes controlled by the energy level of the interface states rather than the work-function difference of the metal and semiconductor. A stronger Fermi level pinning decreases the Schottky barrier height at the interface[67]. Since the Fermi level pinning becomes more prominent as the device junction contact area decreases in size [67], a relatively lower Schottky barrier is expected to be seen on the smaller MoS_2-metal contact junction.

On the other hand, the origin of the rectification behavior could simply be due to the difference of resistance at the two interfaces. To shed more light on the rectification mechanism, the surface potential profile across the flake was taken into consideration. The potential across the device area was obtained using Kelvin probe force microscopy (KPFM). A KPFM scan of a device with asymmetric length/area MoS_2-metal interfaces is shown in Figure 25 a) where an optical image is included in the inset. For clarity, the longer (or larger) and shorter (or smaller) metal-semiconductor contact interface (or area) has

been labeled as left and right respectively. From the KPFM map in Figure 25 a) itself, there is quite a contrast between the surface potential at the two sides.

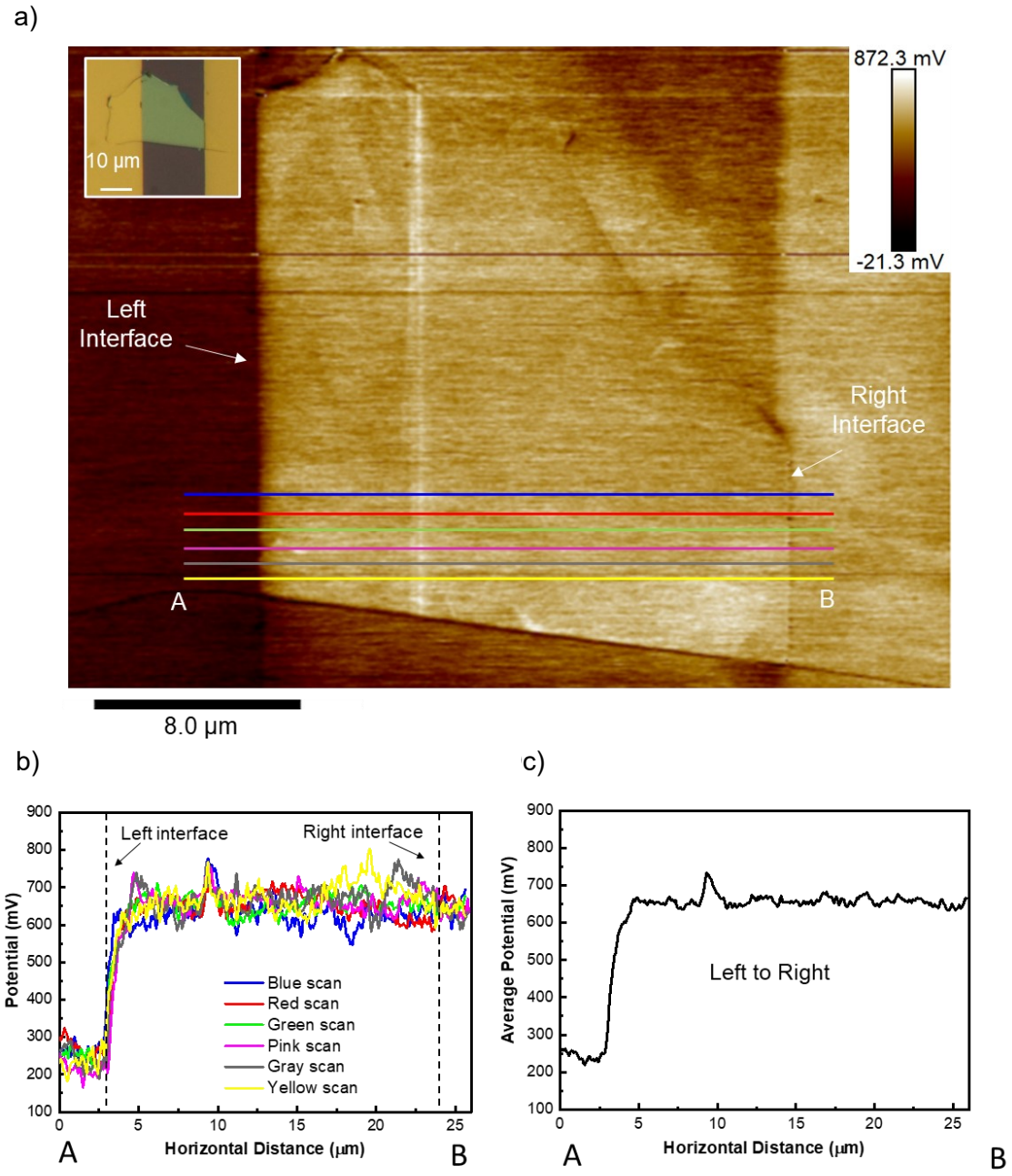

Figure 25: a) KPFM image of an asymmetric area MoS_2 diode with an optical image in the inset. b) surface potential profile across the left and right interface along the lines shown in a). c) Average surface potential profile.

Surface potential profiles along the multiple lines shown in Figure 25 a) across left and right sides are plotted in Figure 25 b). An average surface potential profile obtained

from the data in Figure 25 b) is shown in c). The average surface potential difference (SPD) across the left interface (~400 mV) is significantly higher than the SPD across the interface at right (negligible, displaying no change). The SPD between an AFM tip and the Au or the MoS_2 can be obtained using the following equations:

$$eSPD_{Au} = W_{tip} - W_{Au}, \quad (1)$$

$$eSPD_{MoS2} = W_{tip} - W_{MoS2}, \quad (2)$$

where W_{tip}, W_{Au}, and W_{MoS2} are the work function of the AFM tip, Au electrode and MoS_2 flake, respectively[64, 65].

Figure 26 shows the equivalent circuit resistance along the device. For clarity Figure 26 a) shows the notations of resistance at longer (R_{longer}) and shorter ($R_{shorter}$) MoS_2/Au interfaces on the KPFM scan. The resistance in the bulk MoS_2 is denoted as R_{MoS2} which is assumed to be unchanged during the scan. Figure 26 b) shows the schematic of the equivalent circuit where R_{longer}, R_{MoS2}, and $R_{shorter}$ is connected in series. Assuming that the current flowing across the flake, I, is constant, from the Ohm's law we have;

$$V = I \times R \quad (3)$$

where R is the resistance. If the potential difference at longer interface is V_{longer} and shorter interface is $V_{shorter}$, since $R_{longer} < R_{shorter}$ we have, $I \times R_{longer} < I \times R_{shorter.}$ Alternatively, $V_{longer} < V_{shorter}$. When trying to place these voltages on the diode characteristic I-V curve, shown in Figure 26 c), $V_{shorter}$ falls on the right (compared to V_{longer}) where the junction act as an Ohmic contact. This could explain the KPFM result on Figure 25 a) where the shorter side display no potential barrier since $V_{shorter}$ is large enough to be on the low resistive region. On the other hand, $V_{longer,}$ is lower in magnitude. Therefore, it is possible that V_{longer} is lower than the knee voltage, placing it in the region with a considerable resistance (given by the reciprocal of the slope). This has resulted in a considerable barrier resistance on the longer interface as seen on the KPFM scan.

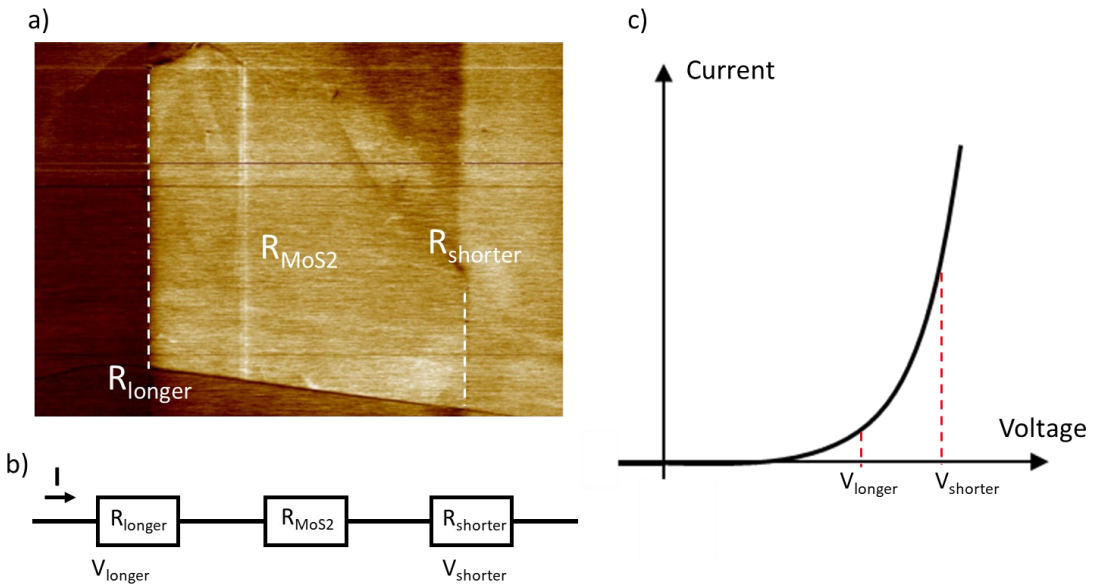

Figure 26: a) Resistance across the sensing area on KPFM scan b) schematic of the equivalent circuit resistance c) diode forward bias characteristic I-V curve.

Once the electrodes were fabricated on the exfoliated MoS_2 flakes, the device was passivated by depositing Al_2O_3 on top. Figure 27 depicts the fabrication process steps incorporating one-step Al_2O_3 passivation. The Al_2O_3 passivation was similar to the process illustrated in Figure 18 except the thickness of the Al_2O_3 layer was maintained at 15 nm and there was no etching involved to expose the flake at the end since the amine-ended aptamers are better immobilized on Al_2O_3 than on MoS_2 surface itself.

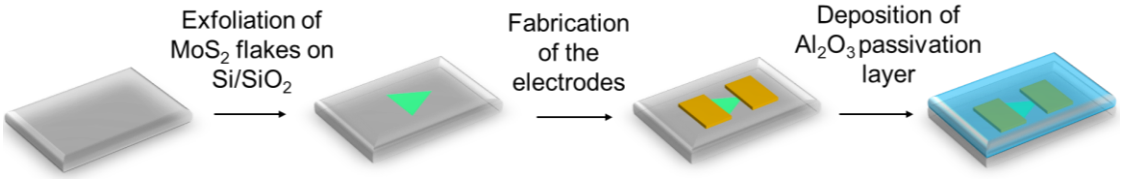

Figure 27: Fabrication process with one-step Al_2O_3 passivation layer.

Each device was initially tested in air and PBS to confirm the quality of the Al_2O_3 passivation before proceeding with functionalization. Figure 28 illustrates the I-V response of device 6 (D6) in air and while PBS has been introduced in the sensing area. There is no significant difference between the two responses, confirming that the Al_2O_3 passivation was successful.

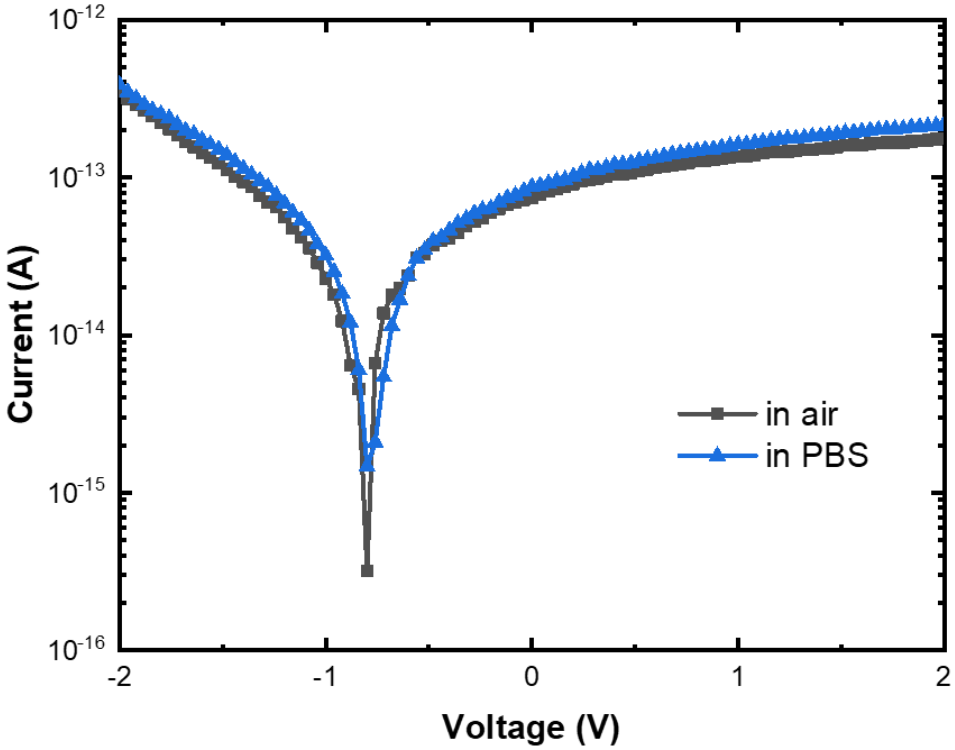

Figure 28 : I-V response of a device with one-step Al_2O_3 passivation (15 nm) (Device 6), before functionalization.

For the CDS, the amine ended aptamers with the VR11 sequence (/5AmMC6/TGG TGG ATG GCG CAG TCG GCG ACA /36-FAM/) were employed as the receptor. For aptamer functionalization, a method reported by Potyrailo R. A. et al. was employed where a change in the chemical composition on the surface at each step during the functionalization has been illustrated [36]. They reported the method for a SiO_2 surface. We were able to replicate the same result on Al_2O_3 surface by following a similar procedure.

The pristine diode sensor with an Al_2O_3 passivation layer was submerged in a aqueous solution of GOPS (10 %) (pH was maintained at 3.5 using HCL). After degassing for 10 min (using Nitrogen (N_2)), the reaction was allowed to proceed at 90 ^{0}C for 4 hours (hr) with occasional shaking[36]. Afterwards, the devices were washed with acetone and 2-propanol. And then dried in an oven (60 ^{0}C) overnight. The surface was activated by submerging the devices in CDI in dry acetonitrile and shaking the solution (1.5 h at 20 °C). The devices were rinsed well with N-free water.

Once the surface has been activated, the device is submerged them in an aptamer sample in order to facilitate aptamer coupling. After receiving the amine-modified ssDNA aptamer, the sample was reconstituted in diluted PBS (100 μM) and aliquoted to 50 μl volumes, which were then stored at -20 ^{0}C as per the manufacturer's instructions. For functionalization, 2 ml of 10 μM aptamer solution was prepared using the stored samples. The activated devices were then submerged in them for 24 hr - 48 hr. Unreacted aptamers were rinsed away by spraying N-free water and dried with N_2. Once dried, they were stored at -20 ^{0}C until measurement in cytokine [36].

All the cytokines which were used in this study (Recombinant Human TNF-α Protein, Recombinant Human C-Reactive Protein, and Recombinant Human IL-6 Protein) were purchased from R&D systems. The as-received TNF-α cytokine samples were reconstituted to a concentration of 25 μg/ml and aliquoted to 20 μl volumes which were then stored at -20 ^{0}C. A similar method was followed in reconstituting and aliquoting IL-6 cytokine. C-reactive protein was reconstituted at a concentration of 6μg/ml and aliquoted to 500 μl volumes for storage at -20 ^{0}C. For the experiments, different cytokine concentrations were prepared using these stored samples by diluting in PBS.

Figure 29 is a plot of the I-V response of D6 as a function of TNF-α concentration. There is a significant change in the I-V curve while the cytokine concentration was increased from 1 pM to 100 nM. In fact, it appears that the rectification of the diode sensor changes with the TNF-α concentration. The change in the rectification factor was used as a figure of merit. Although D6 showed good passivation against PBS and cytokine measurement, later devices showed evidence of oxidization that caused the I-V response to fluctuate in a random manner. To prevent the MoS_2 flakes from oxidizing, the voltage window of the I-V measurement was reduced from -2 V to 2V to -1 V to 1 V interval. Therefore, the rectification factor (RF) has been defined based over the -1 V to 1 V interval as follows:

$$\text{Rectification factor (RF)} = \log | I_{(-1)} | - \log | I_{(1)} | \quad (4)$$

where $I_{(-1)}$ is the current at -1 V and $I_{(1)}$ is the current at 1 V.

Figure 30 is a plot of RF for D6 with TNF-α concentration, where a clear increase can be observed as the concentration is increased. The RF of the device, as define above,

increases with the increasing TNF-α concentration. No oxidization was observed during measurements of D6.

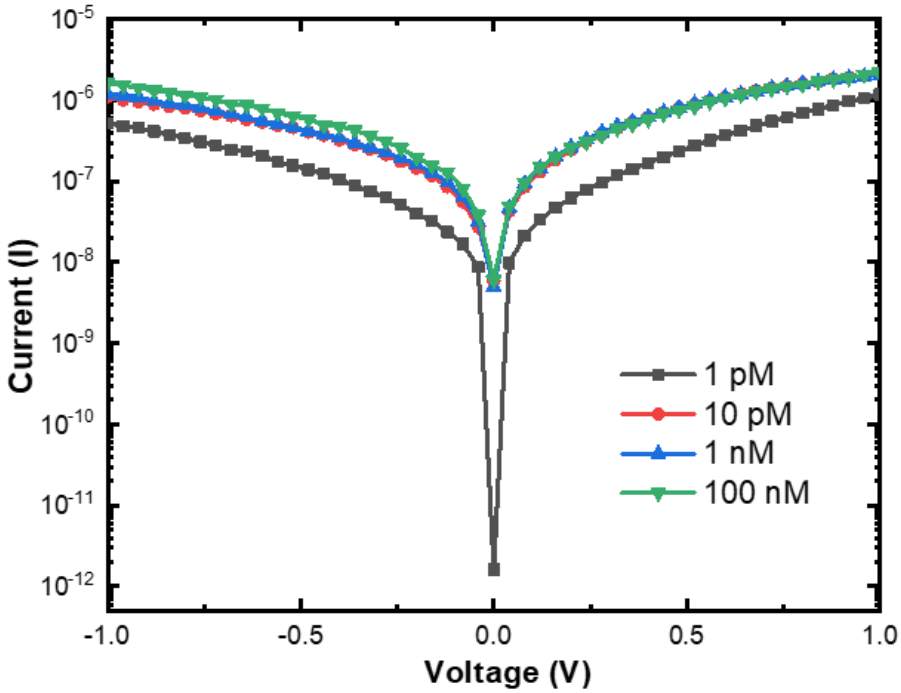

Figure 29: **Plot of characteristics as a function of I-V of D6 TNF-α cytokine concentration.**

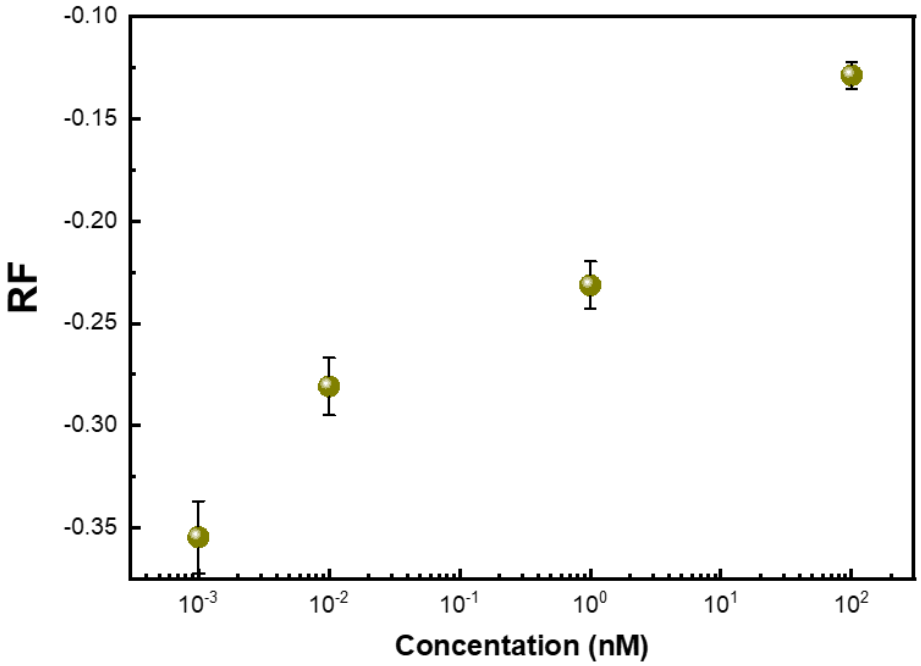

Figure 30: **Plot of RF versus TNF-α concentration.**

Since the absolute value of the current level at -1 V is lower than the current level at 1 V, the rectification factor, as defined above, is a negative value. In order to confirm the trend further, more devices were tested in TNF-α cytokine. For better comparison purposes and to eliminate the device-to-device variation, we define normalized RF as follows

$$\text{Normalized RF} = (RF - RF_{PBS})/(RF_{max} - RF_{PBS}) \quad (5)$$

where RF_{PBS} is the RF corresponding to PBS and RF_{max} is the maximum RF[23].

The next batch of devices fabricated with thick Al_2O_3 passivation layer (15 nm) continued to show oxidization during measurements. Figure 31 shows the discolouring of the flake and the Au contacts that appeared after measurement, due to oxidization.

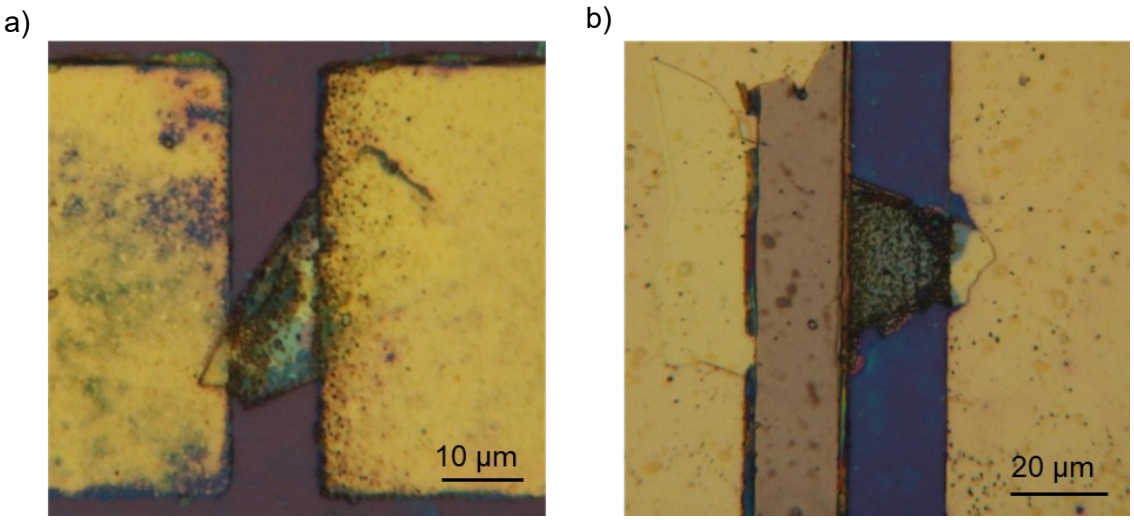

Figure 31: Photographs of oxidized flakes during measurements in PBS. a) Illustrates an MoS_2 flake that has been oxidized during the measurements where a clear discoloring can be seen on both the flake and the electrode area near the flake. b) Another MoS_2 flake that shows oxidization.

In order to mitigate this issue arising due to the failure in the passivation layer, the thickness of the Al_2O_3 passivation layer was increased in subsequent devices until no oxidization was observed. Figure 32 a), b) and c) illustrates the variation of the normalized RF with the TNF-α concentration for Al_2O_3 thicknesses of 20 nm, 30 nm and 40 nm respectively. The normalized RF increased with the increasing cytokine concentration, confirming the overall trend.

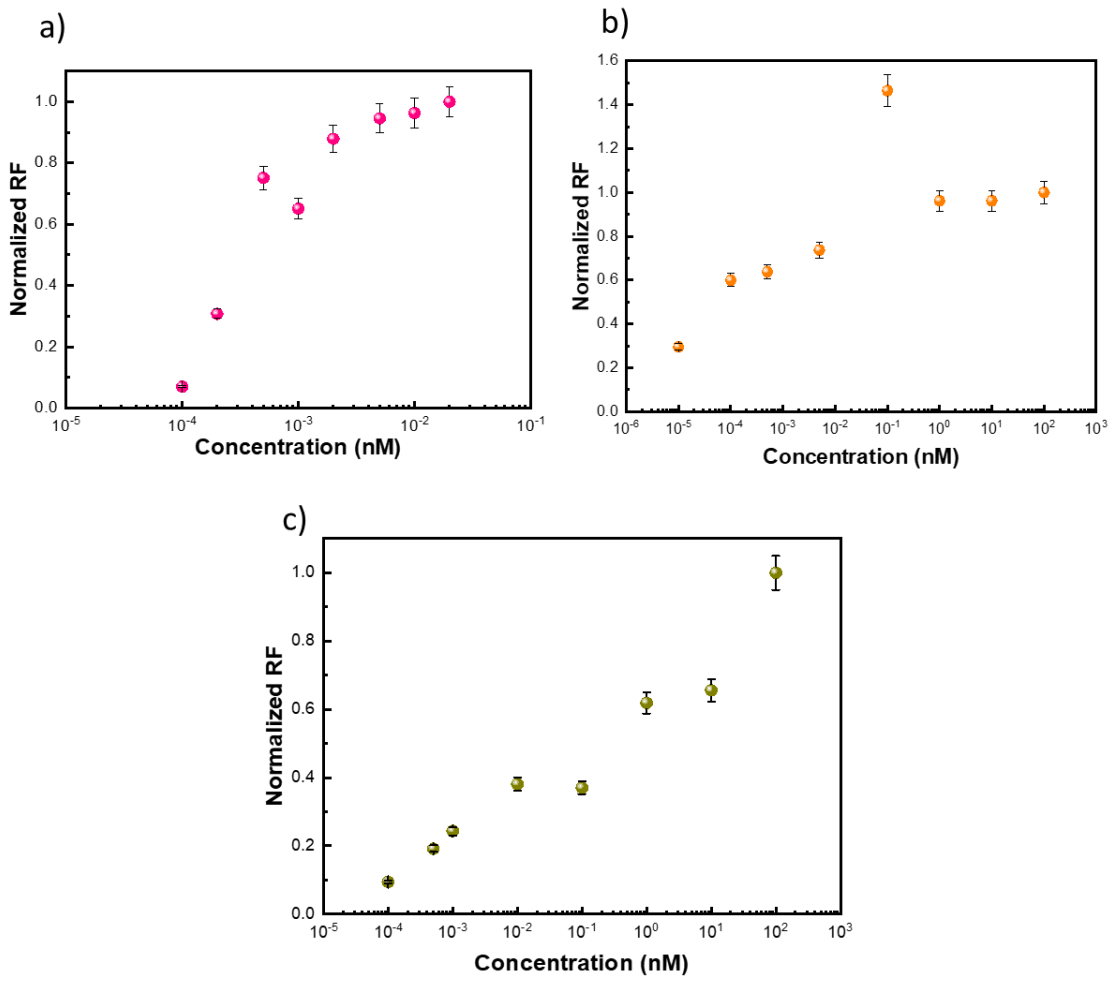

Figure 32: Normalized RF response for devices with one-step Al_2O_3 passivation a) device 7 (D7) (20 nm) b) device 8 (D8) (30 nm) c) device 9 (D9) (40 nm)

As the thickness of the Al_2O_3 was increased, the devices became more resistant to oxidization during I-V measurements in PBS. However, the sensitivity seems to have become compromised. Figure 33 shows the change of I-V characteristic with TNF-α concentration for D9, where the change in the RF with the increased TNF-α concentration not as high as for D6 (Figure 29). Therefore, a better design was required to minimize the oxidization of the flake during measurement without compromising the sensitivity of the CDS. Hence a two-step Al_2O_3 passivation process, where at the first step, a thicker Al_2O_3 layer (70 nm) is deposited in the electrode area and at the second step, a thinner Al_2O_3 layer (5 nm) is deposited in the sensing area.

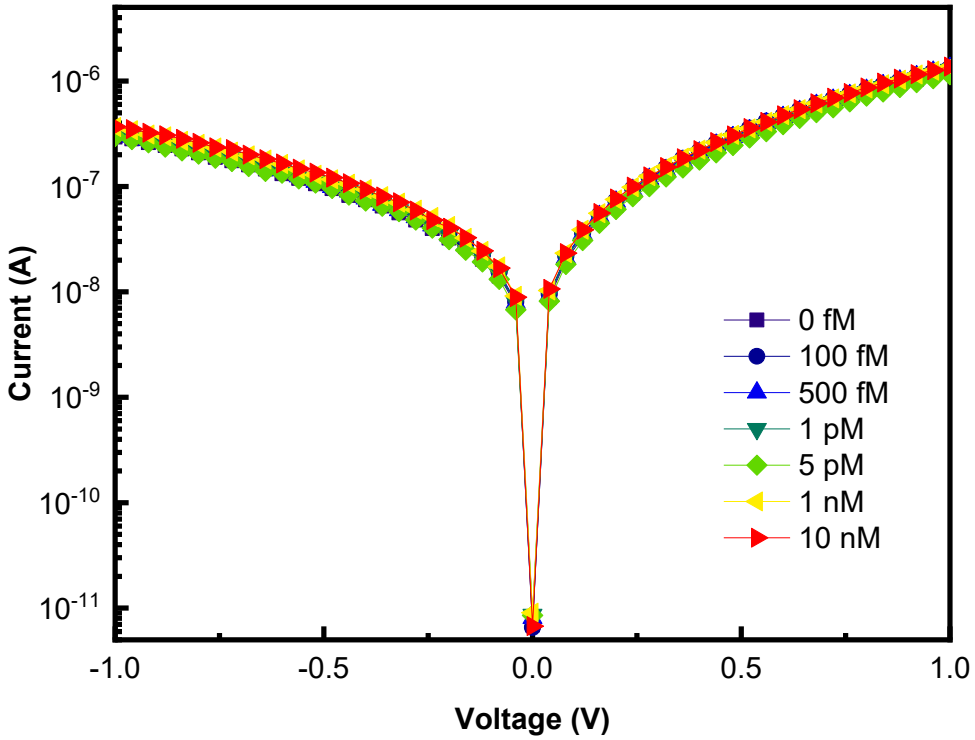

Figure 33: Plot of the I-V characteristics of D9 with an Al_2O_3 layer (40 nm) as a function of TNF-α cytokine concentration.

Figure 34 illustrates the process flow of the two-step Al_2O_3 passivation method. The initial steps are quite similar to the previous one-step passivation method except during the first deposition of Al_2O_3, a thickness of 70 nm is deposited. Then a MoS_2 flake in the sensing area is cleared of Al_2O_3 completely by etching a rectangular stripe in BOE, following a photolithography step. A thinner Al_2O_3 (5 nm) was deposited over the substrate including the sensing area, to facilitate the functionalization to immobilize the aptamers.

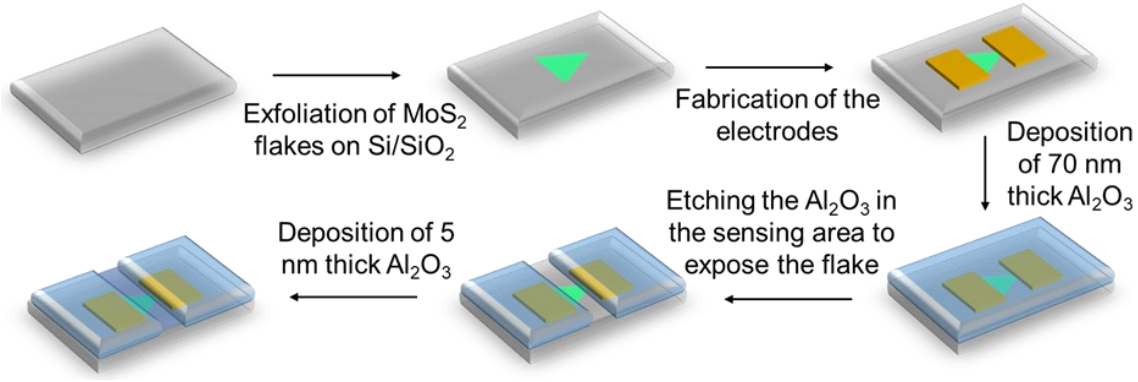

Figure 34: CDS fabrication process with a two-step Al_2O_3 passivation layer.

Figure 35 illustrates an optical image of a device fabricated employing the two-step Al_2O_3 method. The Al_2O_3 thickness on the sensing area (over the flake) is thinner(5 nm) while a thicker layer (75 nm) covers the electrode area.

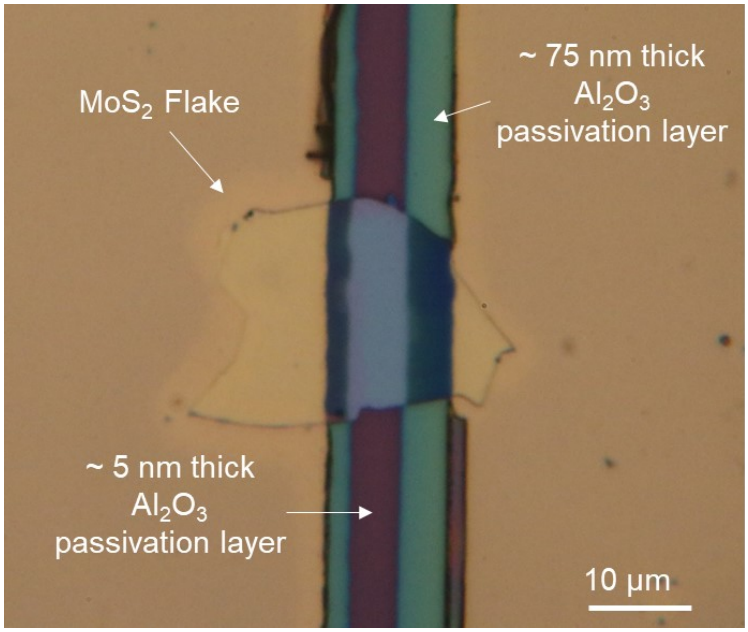

Figure 35: Optical image of a CDS showing the two-step Al_2O_3 passivation.

Many devices fabricated using this two-step method have been tested in PBS and cytokine samples and have shown robust passivation against PBS oxidization during measurement. Therefore, this fabrication process was ultimately followed for the construction of the CDS. All devices tested after this point were fabricated by employing the two-step Al_2O_3 passivation method.

Figure 36 shows a schematic diagram of a cross section of a CDS fabricated by the two-step Al_2O_3 deposition technique. A thicker layer (75 nm) is covering the electrode surface to provide a more robust passivation and a thinner layer (5 nm) over the MoS_2 flake to facilitate the amine-ended aptamer functionalization. Once the devices were fabricated as above, the aptamers were immobilized on the sensing area by flowing the same functionalization method using GOPS and CDI as discussed before.

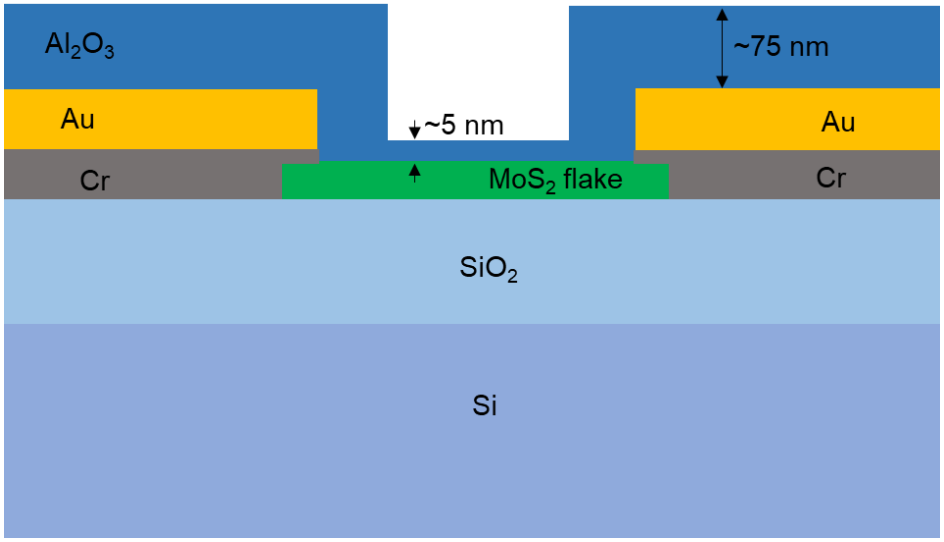

Figure 36: Cross section diagram of the sensing area of the CDS showing a thicker Al_2O_3 layer over the electrode area and a thinner layer over the MoS_2 flake (not to scale).

4.2.2. I-V characteristics obtained for a CDS fabricated with a two-step Al_2O_3 passivation method.

In order to observe the change in the I-V response of a CDS during the functionalization, electrical measurements were carried out at each step of the process. Figure 37 shows I-V measurements obtained for device 10 (D10) during each functionalization step.

The GOPS linker was attached to the Al_2O_3 surface in an aqueous solution at a low pH environment[36]. The GOPS was activated by the attachment of CDI linker[36]. After activating the surface, the TNF-α specific aptamers were anchored on these active sties. The anchoring of the aptamers occurs by the coupling of the amine groups with the activated CDI sites [36]. Figure 37 shows the pristine device (coated with Al_2O_3) initially displayed a rectification of 1.4 order of magnitude. After the GOPS functionalization step, the rectification increased to 1.5 order of magnitude. After the CDI functionalization step the rectification further increased to 1.7 but did not change during the aptamer coupling to the surface. During the functionalization process, the surface of the Al_2O_3 covering the MoS_2 layer is modified at each step. First step of the functionalization involves the hydroxyl groups on Al_2O_3 to react with GOPS where the epoxide ring on the GOPS opens to produce two hydroxyl groups (diol groups) [36]. These diols covalently bonds to the MoS_2 via the Al_2O_3 layer and then react with CDI to create more amine-targeted binding

sites[36]. Possibly due to these surface modifications, there is a change in the surface potential which causes the change in the rectification seen in Fig 37. However, during the final step, the amine-modified aptamers in a PBS solution are just coupled to the CDI moieties hence it does not exercise a strong influence on the overall rectification of the device and did not modify the I-V response significantly.

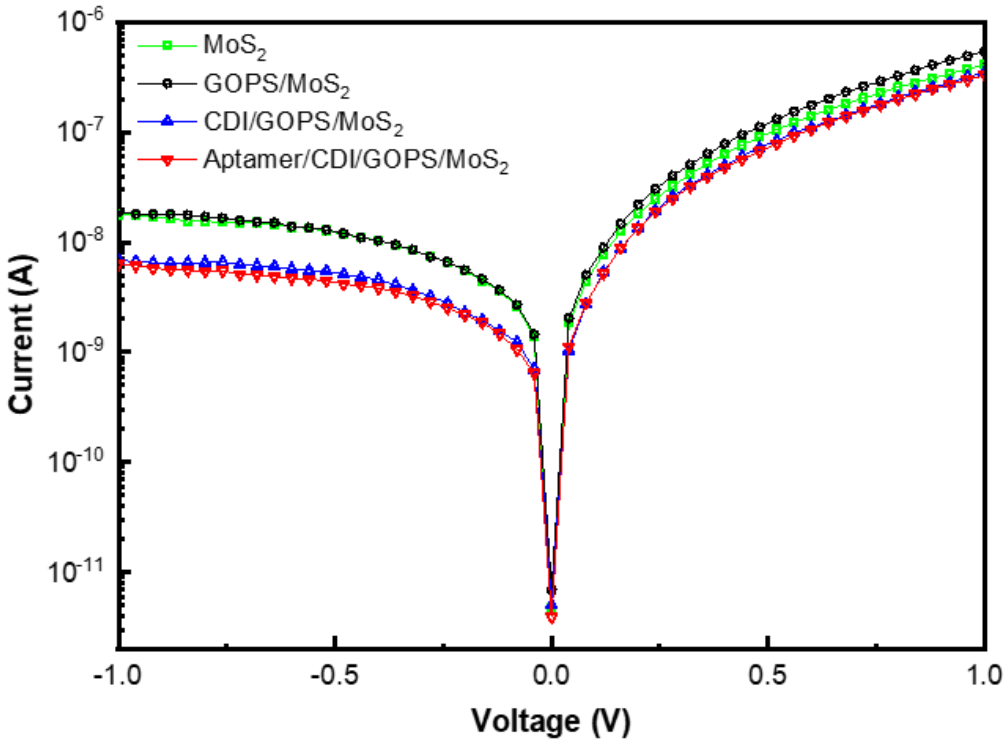

Figure 37: I-V response as a function of steps to functionalize a device.

The TNF-α specific aptamers were modified with a florescence tag (FAM) which has a peak fluorescence response at 525 nm. The fluorescent measurements were carried out by employing a fluorescence imaging spectrometer (HORIBA iHR 320) with an excitation laser wavelength at 485 nm. The data was acquired using a 10X objective lens. The acquisition time was set at 10 seconds (s) with 3 accumulations. The range of the spectrum was selected to be from 490 nm to 650 nm with a step size of 2 nm.

Figure 38 shows the fluorescence intensity variation versus the wavelength before and after aptamer attachment. After the aptamer attachment, the fluorescent tag gives a peak emission of 525 nm wavelength clearly absent in the bare sample. Once the successful immobilization of the aptamers on the devices were verified by observation of

florescence, the devices were tested for the detection of TNF-α. A broader range of cytokine concentration ranging from 10 fM to 100 nM was tested.

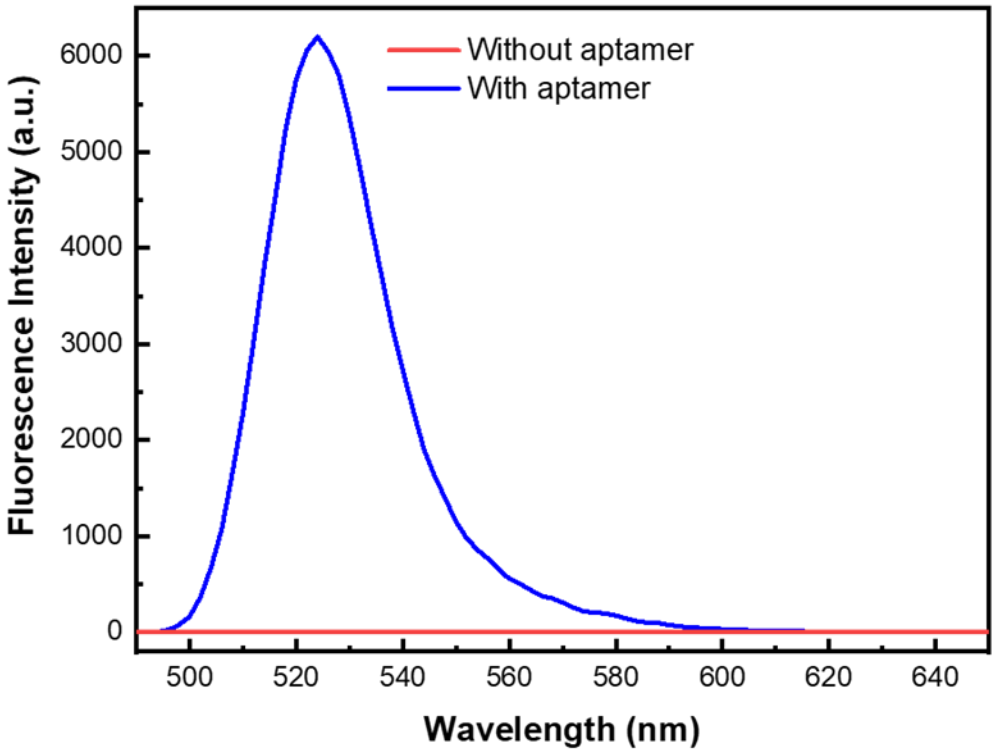

Figure 38: Plot of fluorescence intensity versus wavelength with and without aptamer attached.

Figure 39 shows a plot of the I-V response of D 10 with variation in TNF-α concentration. The current level of the device increases with increasing TNF-α concentration compatible with the observation of devices fabricated with one-step Al_2O_3 passivation method. The trend is more prominent in the linear scale as shown in Figure 40 where a change in the rectification occurs as the cytokine concentration is increased. Assuming that there was a uniform coverage of aptamers over the sensing area, a crude estimation for the total number of cytokines that can attached on the sensing area was calculated. According to the VR11 aptamer data sheet, the length of the aptamer is 8.8 nm. Upon binding of the cytokine, the aptamer may take a compact form (G-quadruplex) [22, 23]. Based on the length, the largest radius this compact form could have is 1.4 nm with a circular area of 6.158×10^{-18} nm^2. Since D 10 has a sensing area (over the 5 nm Al_2O_3 passivation) of 31×10^6 nm^2, a total number of 5.03×10^{24} cytokines can be attached.

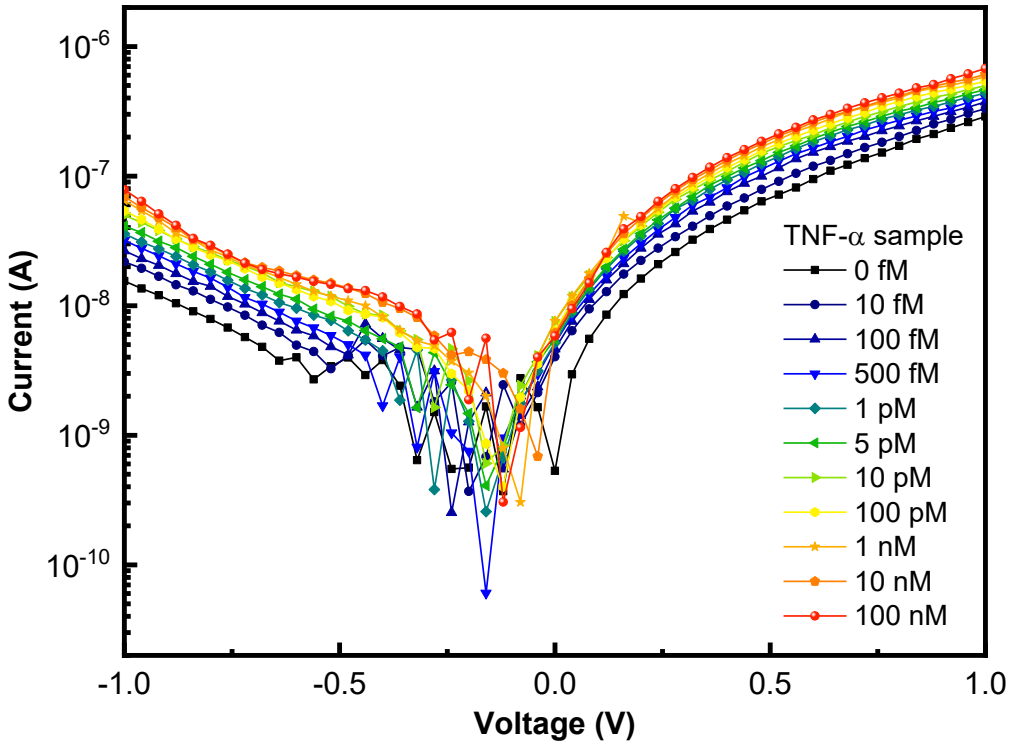

Figure 39: **I-V response of D10 during interaction with different concentrations of TNF-α cytokine.**

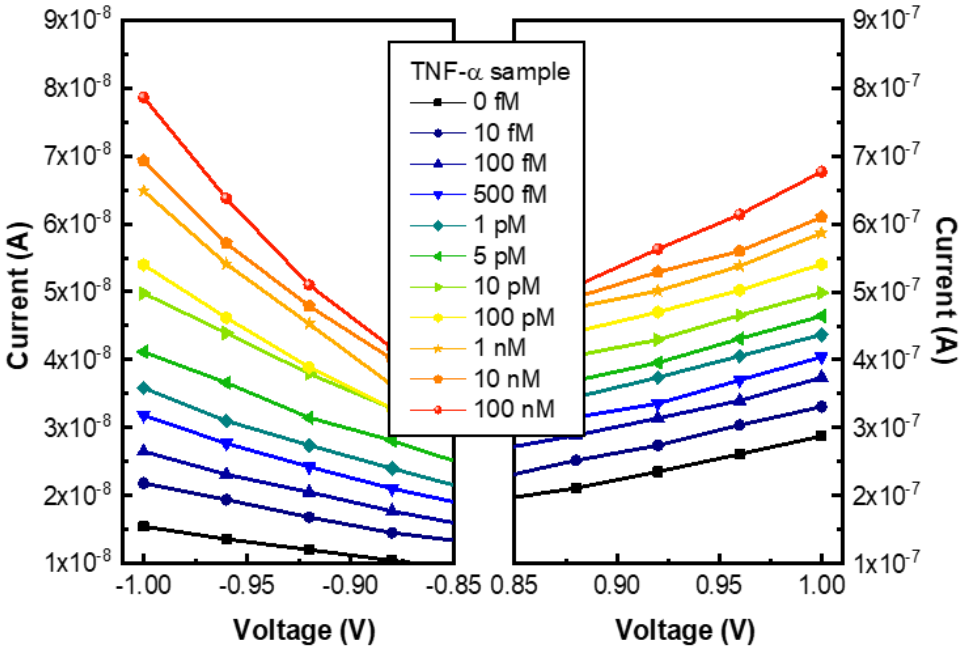

Figure 40: **Plot of the I-V response of D10 in a linear scale, highlighting the change in the RF with increase of TNF-α cytokine concentration.**

Figure 41 is a plot of the normalized RF as a function of TNF-α cytokine concentration. The data points were fit using a classical Hill equation:

$$y = A1 + \frac{A2-A1}{1+10^{(\log(x0)-x)p}}, \quad (6)$$

where A1 = 0 is the bottom asymptote, A2 = 1.05 ± 0.02 is the top asymptote, log x0 = -3.08 ± 0.10 is the center of x data and p = 0.26 ± 0.02 is the hill slope. A reduced χ^2 of 0.0003 was obtained for the fit which indicates a good relation between the TNF-α concentration and the RF. One of the main observations in Figure 41 is that this novel mechanism is capable of detecting TNF-α concentration as low as 10 fM (0.171 pg/ml). This has been identified as one of the key strengths of this CDS. Its lower fM detection capabilities make it a suitable candidate for diagnosis, even of a slight increase in TNF-α in normal human blood serum. That capability would allow the early detection of many diseases that are linked to abnormal increase in cytokine levels. The sensor seems to have reached a saturation point at 1 nM where the Normalized RF did not change significantly with the increase of TNF-α afterwards. This is probably due to the binding sites been exhausted with the addition of TNF-α.

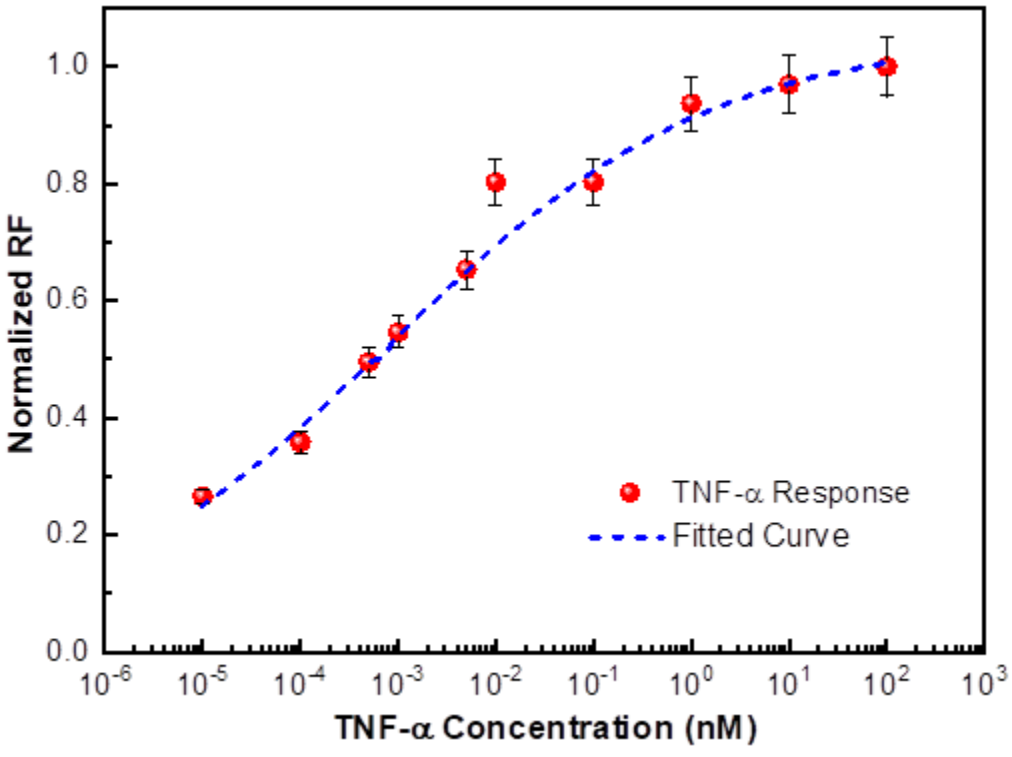

Figure 41: Plot of the normalized RF versus the TNF-α concentration for D10.

4.2.3. Detection mechanism.

In this work, the cytokines were introduced to the sensor in a 1X PBS buffer media (pH 7). Interestingly in this buffer TNF-α cytokine is deemed to be charged negatively[22, 23]. Therefore, when the cytokines bind to the TNF-α specific aptamers, a stable and compact G-quadruplex may form [22, 23]. This brings the negatively charged cytokine closer to the Al_2O_3 surface and to the electron-rich aptamer. This would increase the negative charge on the Al_2O_3 surface and induce a gating effect on the MoS_2 sensing layer beneath, resulting in a change in the rectification[22, 23]. Figure 42 shows a schematic of the attachment of TNF-α cytokine to an aptamer which result in an increase of negative charge concentration on the sensor surface.

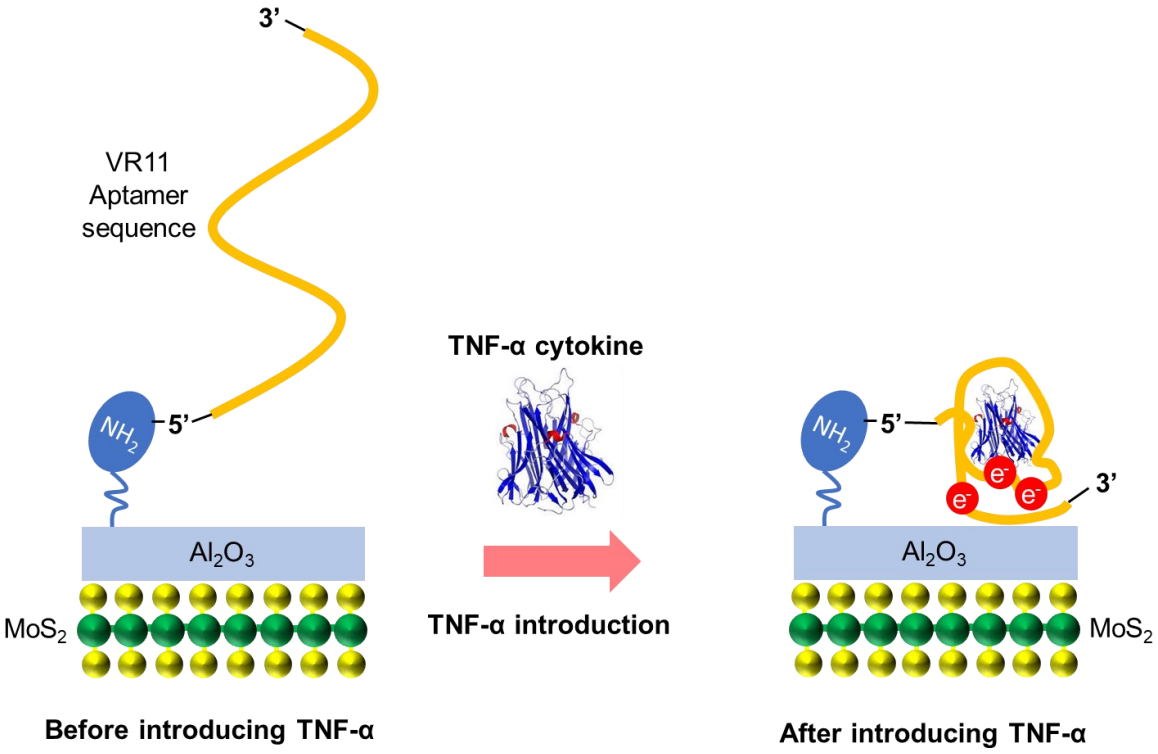

Figure 42: Schematic of the attachment of TNF-α cytokine with an aptamer. (Source: The schematic of the TNF-α was downloaded from https://en.wikipedia.org/wiki/Tumor_necrosis_factor#/media/File:TNFa_Crystal_Structure.rsh.png where the author has released the artwork to the public domain)

In order to further verify this proposed mechanism, a liquid gating measurement experiment was conducted as shown in Figure 43. The V_{GS} is the gate bias applied via a pure PBS droplet (without any cytokine) on the sensing area which is also identified as

the liquid gate voltage (V_{GS}). The voltage between drain and source is denoted as V_{DS}, which was swept between -1 V to 1 V for each V_{GS} while measuring the current across the drain and source (I_{DS})

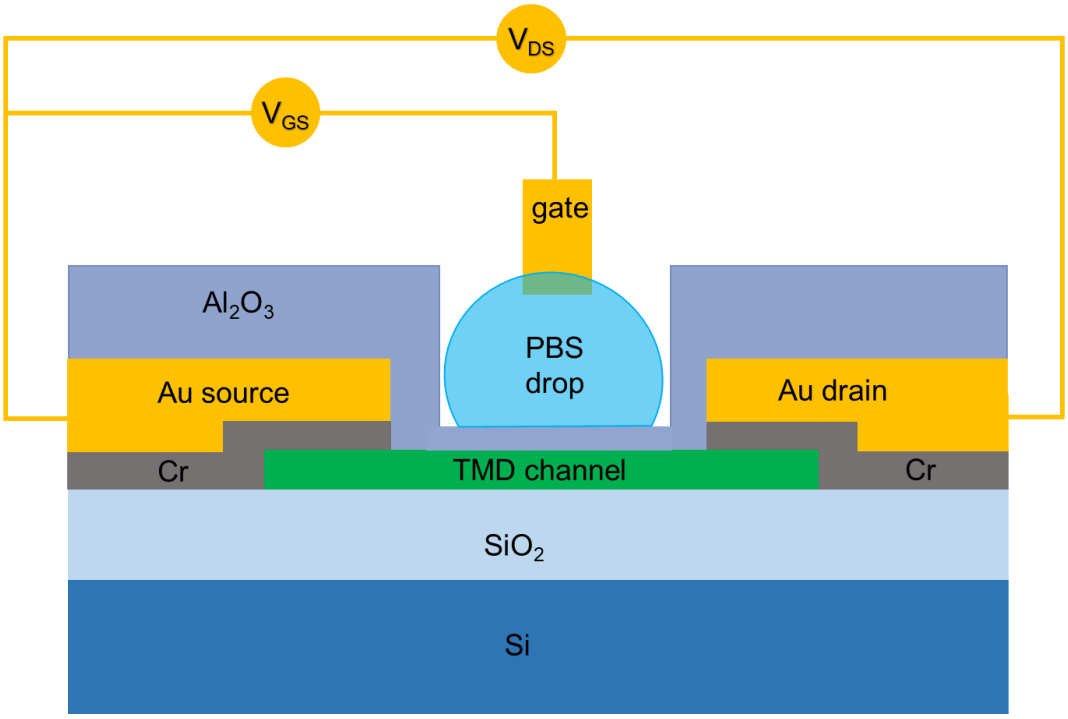

Figure 43: Schematic of the liquid gating setup.

Figure 44 shows plots of the I-V response across the drain and source (I_{DS}) obtained for a CDS under increasing negative liquid gate voltage (V_{GS}) from 0 V to -1 V, applied via a PBS droplet on the sensing area. A different device (D11) was employed for liquid gating testing. D11 was fabricated similarly to D10, employed the two-step passivation process. Figure 45 shows the variation of normalized RF as a function of negative V_{GS} for D11. The trend is similar to the observation seen during interaction with TNF-α cytokine. This observation further confirms that the binding of the TNF-α cytokine to the aptamer prompts a gating effect on the MoS_2 sensing layer, which induces a change in the rectification.

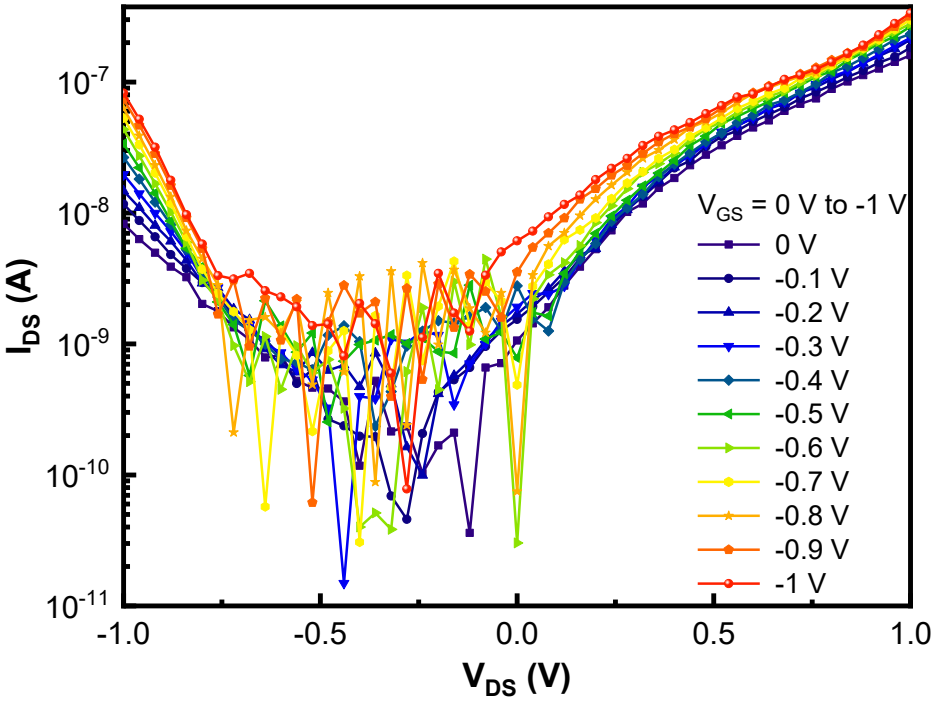

Figure 44: **I_{DS} versus V_{DS} for different gate voltages ranging from 0 V to -1 V at an increment of -0.1 V at each step.**

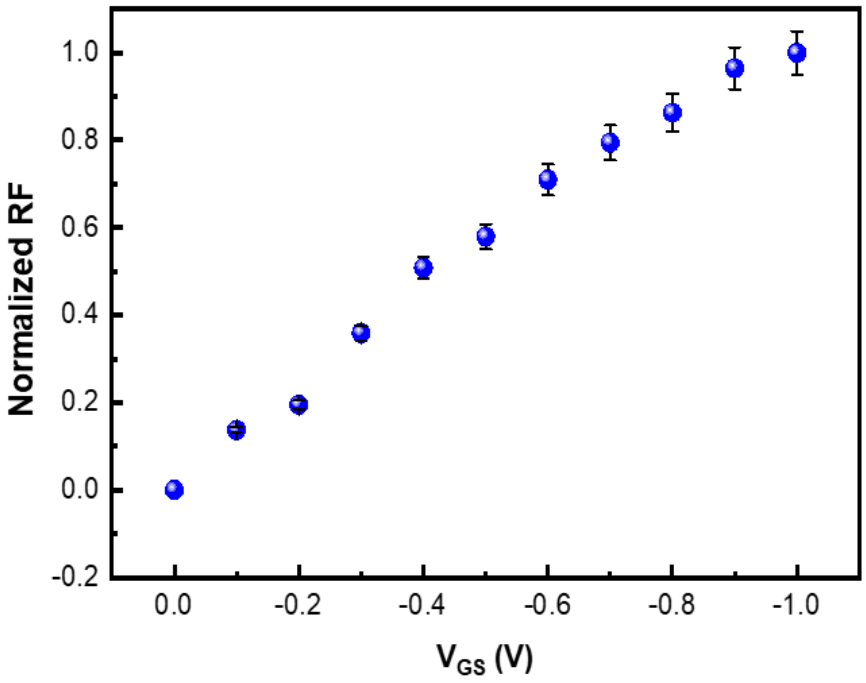

Figure 45: **Plot of normalized RF versus negative V_{GS} for D11.**

Another noticeable observation in the I-V response of Figure 39 (also Figure 44) is the increase in the current level with increase of TNF-α concentration (also with negative

gate voltage).Conventionally, for n-type materials such as MoS_2, a negative gate voltage prompts a decrease in current[45]. Specifically for CVD grown MoS_2 flakes where defects due to sulfur (S) vacancies are in abundance (which further enhanced the n-type behavior), this is always the case [68]. However, in mechanically exfoliated thin MoS_2 flakes, where there is less S deficiency, an enhanced p-channel with more balanced ambipolar transportation can be realized[69]. In fact, Ye T. J. et al. and Zhang Y. et al. have demonstrated ambipolar operation in MoS_2 by observing hole conductivity (additional to the conventional electron transportation) via liquid gating where an increase in the current level was seen with increase of the negative liquid gate voltage[69, 70]. Similar to these observations, the increase in the current level with the cytokine concentrations or negative voltage seen in the CDS suggests the existence of ambipolar transport nature in thin MoS_2 flakes used in this study. Since the intrinsic rectification was attributed to difference of the leakage current at two interfaces ($I_{LS} < I_{LL}$), it can be argued that due to the gating effect exercise by TNF-α, both I_{LS} and I_{LL} levels were increase. But the magnitude of the increment of I_{LS} is greater than I_{LL}.

In order to investigate the specificity of the CDS, D10 was tested against two other non-target cytokines, IL- 6 and C-reactive protein, which are common biomolecules present in blood serums used as negative controls. The CDS was tested for these control proteins under the same conditions as TNF-α. A bar graph of normalized RF for different control protein concentrations alongside the TNF-α, is plotted in Figure 46. For the non-specific IL-6 cytokine, the response of the CDS was quite minimal as the normalized RF was close to zero even at higher concentrations showing a good selectivity. On the contrary, the non-specific C-reactive protein showed a noticeable response, specially at higher concentrations. Still, the highest response observed for C-reactive protein was 3.2 times lower than the TNF-α cytokine response at the same concentration.

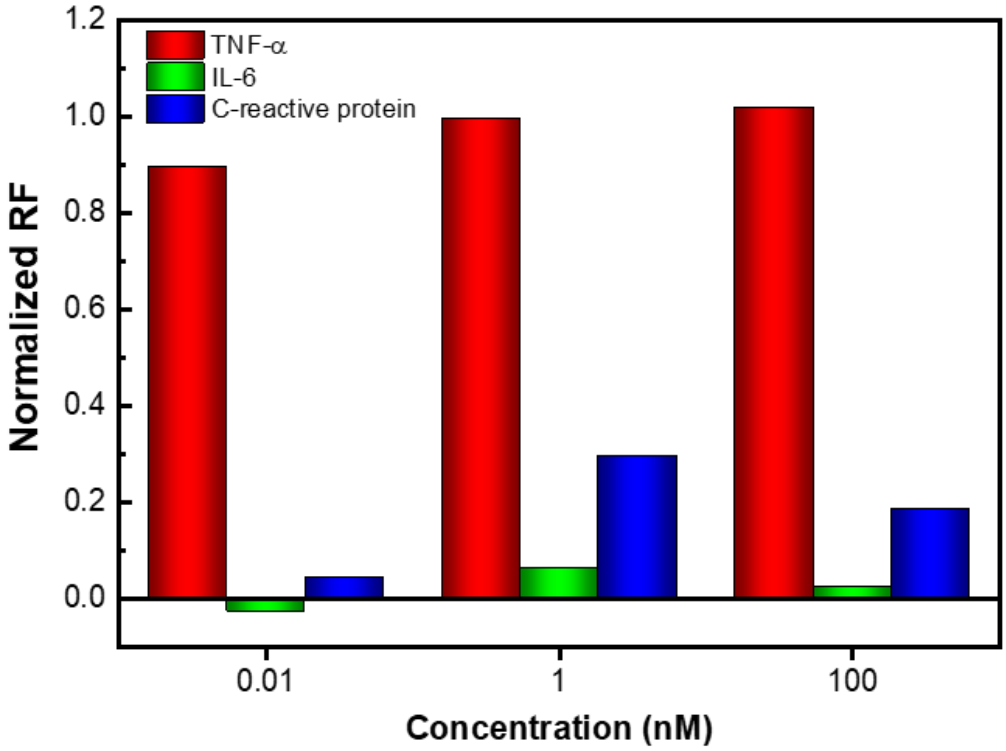

Figure 46: Normalized RF as a function of non-targeted cytokines, IL-6 and C-reactive protein compared to TNF-α.

A possible cause of the lower specificity seen in C-reactive could be its' higher molecular weight, which causes a considerable number of proteins to reach the sensing area without actually being bound to the aptamer. The MoS_2 flake is quite sensitive to the surface charge on the Al_2O_3 layer. A similar behavior has been reported by Fathi-Hafshejani P. et al for a WSe_2 based FET for detection of covid-19 virus, functionalized with a continuous layer of 2.7 nm long linker, directly on the WSe_2 surface, that showed a considerable response to pure ionic liquid (negative control)[35]. It is possible that the rectification of the CDS is affected by the heavy C-reactive proteins that reaches the sensing area. However, considering the overall picture, the negative control tests indicate that the aptamer used in this study shows adequate specificity to TNF-α cytokine.

To verify that the response observed in the CDS is in fact due to the successful binding of the TNF-α cytokine to the aptamer, a secondary negative control test was carried out incorporating a device without the presence of aptamers (a separate device D11). This control device was only activated using GOPS and CDI linkers but was not allowed to interact with the aptamers. Figure 47 shows a plot of normalized response of the control device compared with a CDS properly functionalized with aptamer, for different

TNF-α concentrations. A stark contrast can be seen between the two responses where the RF of the CDS changes with the TNF-α cytokine while the control device's response only fluctuates around the zero level (shown with a dash line) hence confirms the CDS response is due to the effective interaction between TNF-α cytokines and the aptamers.

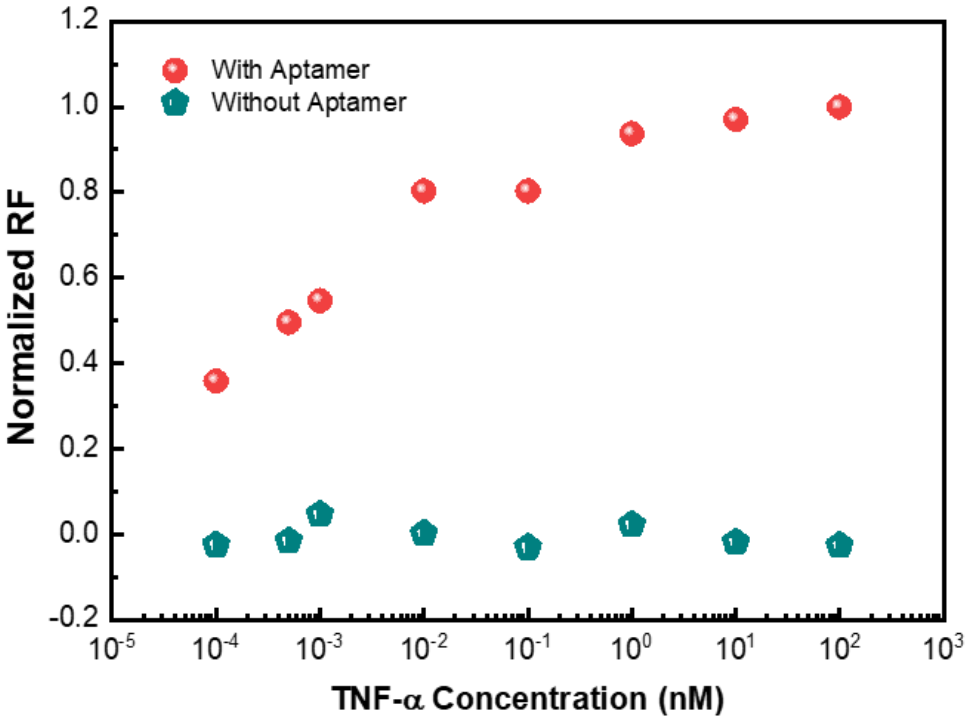

Figure 47: Plot of normalized RF versus TNF-α concentration for a device without aptamers showing no trend compared to a CDS with aptamers present.

The general trend of the RF with the TNF-α concentration where the RF increases with the increasing TNF-α concentration was further confirmed by testing more CDS, D12 and D13 and as shown in Figure 48.

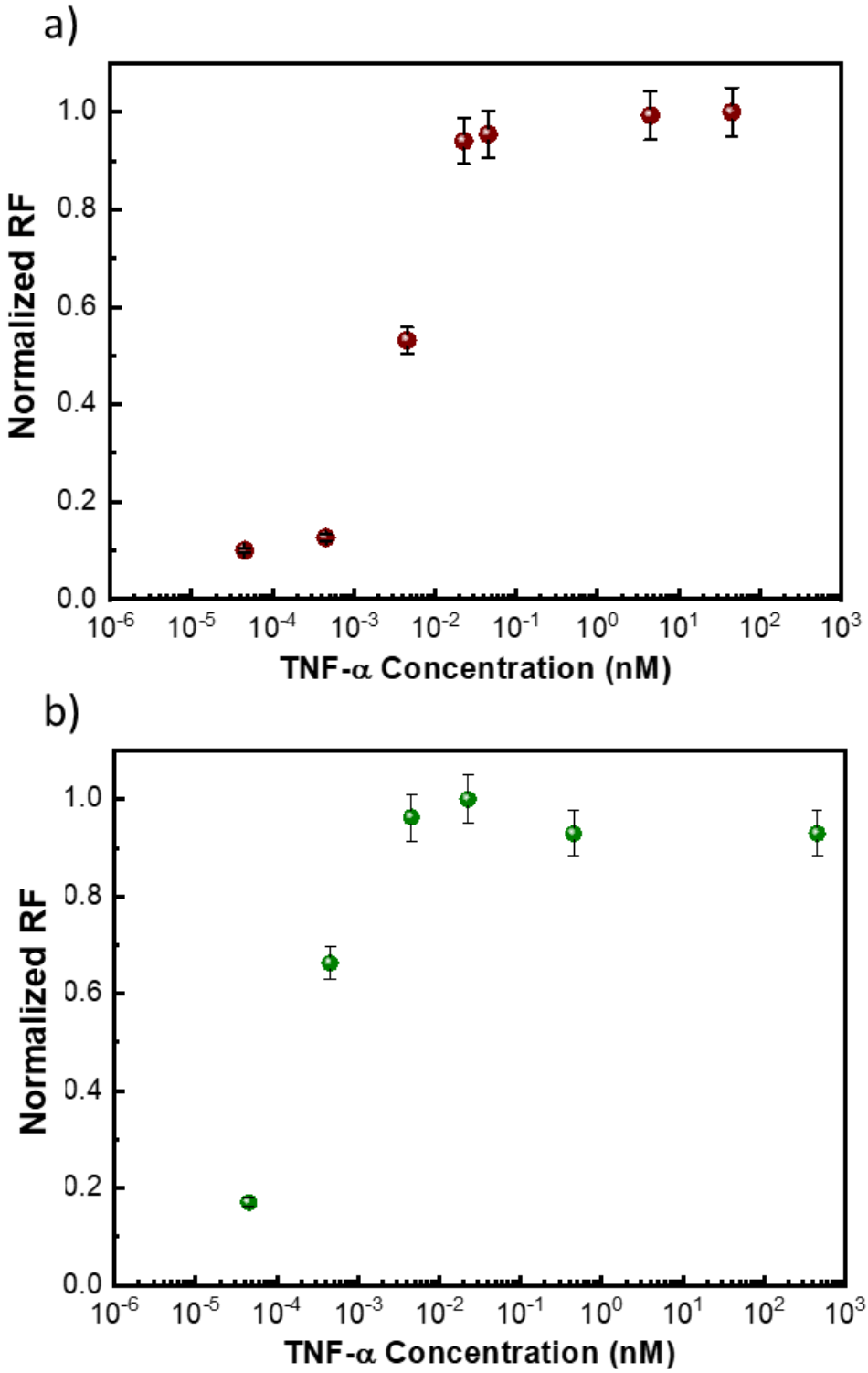

Figure 48: **Plot of the normalized RF versus the TNF-α concentration for a) D12 and b) D13 (fabricated similar to D10).**

Each experiment has been repeated a few times, on a fresh device each time. This is because unlike gas sensors, the biosensors are for one time use only, unless the sensing area can be cleared from the bounded target molecules [35]. All CDS were fabricated employing exfoliated MoS_2 flakes. A major disadvantage of using exfoliated flakes is that we do not have a control over their dimensions and the shape of the flakes. Therefore, each device possessed a different initial rectification factor resulting in a varying response from device to device. Figure 48 shows the plot of Normalized RF versus TNF-α concentration for more devices as a confirmation of the repeatability of the trend. However, due to the difference in the rectification at the pristine stage, the linear ranges, and the saturation points were different from device to device. Therefore, it was not possible to generalize the trend for multiple devices which prevented us from calculating a mean and standard error.

Another sensor based on CVD-grown WSe_2 for the detection of covid has reported that, due to the device to device variation it was not possible to generalize the trend[35]. They have reported that due to the difference in the distribution and the number of flakes on each device, the starting current levels and the change of the figure of merit with increase of target were different from device to device [35]. Hence the standard deviation calculations are not valid since the responses were not at the same scale. Nevertheless, they showed that the trend for the figure of merit is similar (increases with increasing target concentration) and have shown a proof of concept device.

We have performed selectivity tests for non-targeted cytokines also on fresh batch of devices functionalized in a similar way as were D10, D12 and D13 by immobilizing the TNF-α specific cytokines. Figure 49 shows a comparison of the normalized RF for TNF-α which were measured on D10, IL-6 which was measured on a fresh device D14, and C-reactive protein measured on another fresh device D15. For better comparison, after baseline correction the data using the RF measured in pure PBS, they were normalized according to the maximum RF measured for TNF-α on D10. As seen in Figure 49, TNF-α specific aptamer shows good selectivity against IL-6 and C-reactive, even on freshly functionalized devices. The inverted response for IL-6 observed at 0.01 nM could be a measurement artifact.

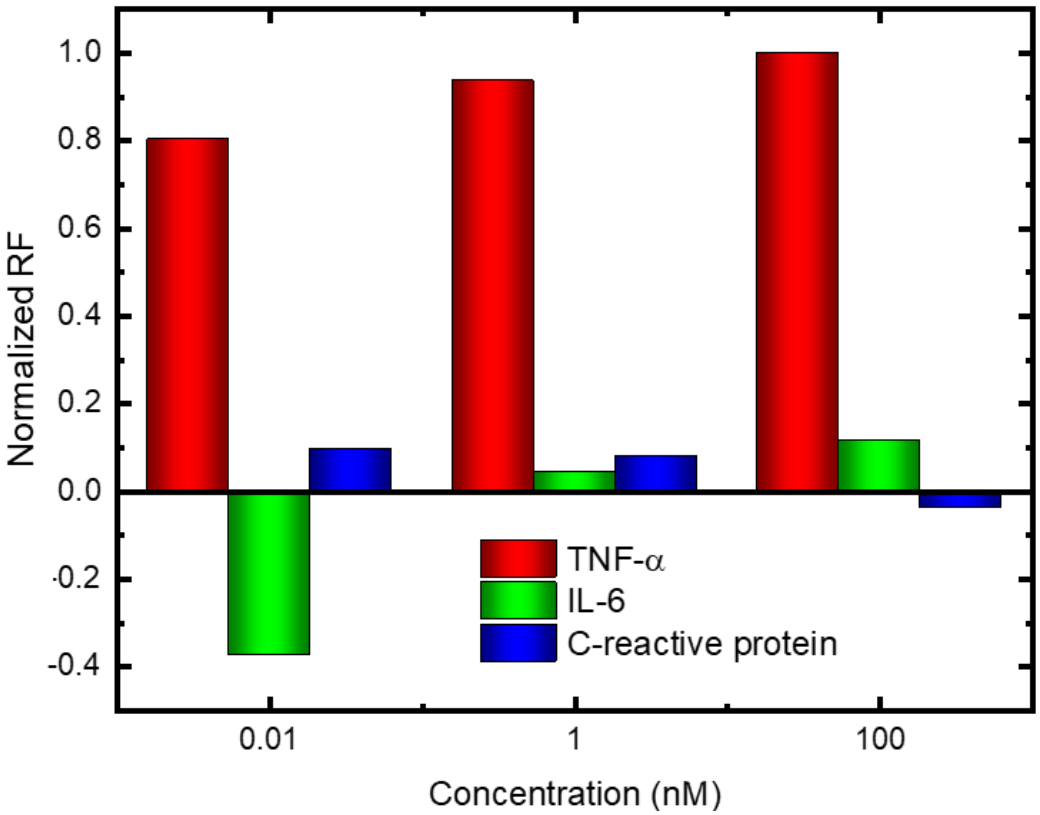

Figure 49: **Bar graph of normalized RF versus concentration IL-6 and C-reactive protein on fresh devices compared to TNF-α.**

Chapter 5. Conclusion and Future Work

In this study, we have for the first time demonstrated a cytokine sensor based on an asymmetric MoS_2 diode. The CDS was tested for detection of TNF-α, which showed an ultra-high sensitivity to the targeted cytokine (10 fM) one order of magnitude lower than the Enzyme-linked immunosorbent assay (ELISA) method, which is the gold standard for cytokine detection[71]. Generally, in ELISA, an antigen is either directly immobilized or by a specific antibody in a microplate well [72]. Next, a 'primary detection antibody' is added, forming an antigen-antibody complex [72]. In the direct detection method, the primary detection antibody is directly labeled with an enzyme. In the indirect detection method, the primary detection antibody attaches to a secondary antibody [72]. The addition of a substrate induces a color signal indicating the presence of the antigen in the sample. The quantity of the antigen in the sample is proportional to the measurement of the optical density [72].

The experimental LOD observed for TNF-α in the present CDS is one order less than the typical range presented among healthy young and adult population (188 fM to 289 fM[10]).Table 3 below summarizes a comparison between the performance of the CDS presented in this work with other reported cytokine sensors.

Table 3: Comparison of this work with reported sensors.

Technique	Sensing Material	Receptor type	Dynamic Range	LOD	Reference
Reflectometric interference spectroscopy	AmiNoAcid (monomer) Decorated	Nano structured TNF-α	-	3.273nM	[73]
QCM	Gold electrode	Antibody	-	1.46nM	[15]
Potentiometric sensor	PVA nano shell	Antibody	-	0.878 nM	[74]
Electrochemical redox spectra	Gold electrode	Aptamer	-	0.319 nM	[75]
Electrochemical redox spectra	Gold electrode	Aptamer	1+ logs	0.292 nM	[76]
Photonic microring resonator	Gold electrode	Antibody	2+ logs	0.269 nM	[77]
Photoluminescence spectroscopy	Quantum dot on the 5 terminus and gold nanoparticle on the 3 terminus	Aptamer	-	99 pM	[13]
Electrochemical	Gold electrode	Aptamer	-	58.5 pM	[78]
FET	Graphene	Aptamer	-	26 pM	[22]
FET	Graphene	Aptamer	-	5 pM	[23]
FET	Graphene	Aptamer	-	2.75 pM	[79]
Localized-surface plasmon resonance (LSPR)	gold nanorod	Antibody	-	0.59 pM	[80]
Electrochemical	Indium tin oxide	Antibody	1+ logs	0.59 pM	[81]
Electrochemical	graphene oxides	Antibody	-	0.29 pM	[82]
Electrochemical impedance	TiO_2 nanotube	Antibody	~3 logs	0.29 pM	[83]
FET	MoS_2	Antibody	-	60 fM	[26]
Electrochemical	gold electrodes	Antibody	1+ logs	58.5 fM	[84]
Photoelectrochemical	TiO_2 nanorod and ZnS nanoparticle	Antibody	-	58.5 fM	[20]
Capacitance electrochemical	silicon nitride	Antibody	1+ logs	58.5 fM	[19]
Diode sensor	MoS_2	Aptamer	~ 5 logs	10 fM	This Work

Since late 2019 due to the COVID-19 pandemic, research on developing early diagnostic sensors has accelerated tenfold, enabling lower cytokine detection limits. However, most of these techniques require post data processing which lengthens the overall detection time. For example, sensors based on optical or electrochemical measurements need more time consuming data processing before they can be used for diagnosis purposes. Apart from that, some of the sensors have used complex synthesis or fabrication techniques which could be inaccessible to a wider population. On the other hand, the proposed CDS is based on a simpler detection mechanism and even simpler fabrication method that is compatible with current microfabrication techniques for mass production[12]. Furthermore, we have incorporated aptamers as the receptor type which allowed us to employ a functionalization process based on silane chemistry via GOPS interacting together with CDI, which uses the least toxic chemicals that are cheaper than other, more toxic alternatives[36-38].

We attribute the ability of achieving lower LOD with the CDS (as low as 10 fM) to the nature of the device structure thicker passivation layer (75 nm) over the electrode area, minimized the effect from leakage current and a thinner passivation layer (5 nm) over the sensing area enhanced the sensitivity in the MoS_2 layer. This hypothesis was made based on another study on a MoS_2 FET for TNF-α cytokine detection with a lower LOD that had employed a similar device structure to mitigate the interference from leakage current [26]. Our initial device fabrication process only contained a single passivation step to cover the sensing area, as well as the gold electrodes. However, several devices showed malfunctioning due to the MoS_2 flakes being oxidized during measurement, calling for a thicker passivation layer. To mitigate this issue, the passivation was carried out by a two-step process where a thicker Al_2O_3 layer was deposited to passivate the gold electrodes and a thinner layer over the sensing area used to facilitate the functionalization.

Overall, one of the main challenges in developing cytokine sensor is the hardship of achieving higher sensitivity without compromising the specificity. We believe that this novel sensing mechanism based on the asymmetric MoS_2 diode is more sensitive to surface charge variation occurring due to the interaction of cytokines. For instance, Bartolomeo A. D. et al. have shown a steeper variation in the RF due to negative back gating for a MoS_2 asymmetry FET device[85]. Thinking along these lines, we believe that the proposed sensing mechanism of the CDS can achieve higher sensitivities in detecting negatively-charged cytokines allowing further improvement in the specificity. The

fundamental specificity in the CDS is achieved by the nature of the aptamer. In general, the VR11 has shown high specificity to TNF-α cytokine [22, 23, 45]. However, the specificity could be further improved by using a surface passivation technique to block non-specific binding at the unreacted sites on the sensing area. For example, Potyrailo R. A. has reported ethanolamine solution (0.1 M) can be applied to block non-specific binding which could be used to further enhance the specificity of our CDS[36]. Therefore, improvement to the sensor specificity maybe feasible by employing these surface blocking strategies to further discourage non-specific binding. Also, before the cytokine detection, the sensors should be repeatedly tested in PBS to verify the that the increase in the IV is not an measurement artifact but due to the actual binding events.

Since the mechanism of the present CDS is based on the RF, the RF at the initial level is important. The intrinsic RF of the device is mostly determined by the asymmetric shape of the MoS_2 flake where a triangular shape is highly favorable. Due to the nature of the fabrication process where MoS_2 flakes were obtained by mechanical exfoliate, there is no control over the flake dimension or the shape. Therefore, it was not possible to conduct a study to investigate the impact of the initial RF on the device performance. Even though we used mechanically exfoliated flakes to present this new detection mechanism, it is important to have a precise control over the dimensions of the flake for more accurate and reliable sensors for clinical usage since that would allow us to reproduce devices with similar RF at the pristine condition. Hasani A. et al. has reported a method to synthesize thin film MoS_2 on Si which can be utilized to obtain patterned MoS_2 with triangular shape where a better control over the dimension can be realized[86]. Furthermore, there are other 2-D materials that can be incorporated to fabricate similar CDSs presented in this work. For instance, Miansari M. et al. have employed 2-D multilayer graphene oxide (GO) films for applications in ion transport where the rectification was shown to be increased with enhanced film shape asymmetry[66]. Since GO has been reported to be used for cytokine sensing, this detection mechanism based on the diode behavior could be potentially used for developing cytokine sensors based on a GO diode sensor [82]. Apart from them, other semiconducting materials such as Si or GaAs could be employed as the sensing material. However, these new materials needed to be tested for the sensitivity in detecting cytokines.

Since the receptors used in this study are aptamers, they can be reused by treating it with urea buffer [6]. This is another future study, that can be incorporated in the device

testing phase. Apart from that, after completing one measurement set, the sensor can be cleaned using O_2 plasma and re-functionalized for a new measurement set. Having recyclable sensors are important in the aspect of environmental friendliness.

Once synthesis methods with better control over the flake dimensions has been incorporated, it will be possible to reproduce the same sensing behavior for the devices (with similar performance) which could then be utilized to generalize the response. Due to current limitations for obtaining similar starting MoS_2 flakes, each device needs to be calibrated in PBS to determine the base line. The cytokine response is only presented with respect to the base line measurement in PBS. However, with improved synthesis techniques to achieve uniform devices with similar performance, we believe that one calibration in PBS would be sufficient for all devices.

Our main goal was to present a new mechanism to detect cytokine concentration based on a MoS_2 asymmetric diode sensor. The CDS presented here has shown promising results for rapid detection of lower TNF-α concentrations making it suitable for point-of-care testing with minimal supervision by a health care Professionals.

References

[1] L. Wang, Y. Wang, J. I. Wong, T. Palacios, J. Kong, and H. Y. Yang, "Functionalized MoS_2 nanosheet-based field-effect biosensor for label-free sensitive detection of cancer marker proteins in solution," *Small,* vol. 10, no. 6, pp. 1101-1105, 2014.

[2] Z. Hao, Y. Pan, W. Shao, Q. Lin, and X. Zhao, "Graphene-based fully integrated portable nanosensing system for on-line detection of cytokine biomarkers in saliva," *Biosensors and Bioelectronics,* vol. 134, pp. 16-23, 2019.

[3] C.-A. Vu and W.-Y. Chen, "Field-effect transistor biosensors for biomedical applications: recent advances and future prospects," *Sensors,* vol. 19, no. 19, p. 4214, 2019.

[4] A. Geldert, X. Zhang, H. Zhang, and C. T. Lim, "Enhancing the sensing specificity of a MoS 2 nanosheet-based FRET aptasensor using a surface blocking strategy," *Analyst,* vol. 142, no. 14, pp. 2570-2577, 2017.

[5] S. Guo and S. Dong, "Biomolecule-nanoparticle hybrids for electrochemical biosensors," *TrAC Trends in Analytical Chemistry,* vol. 28, no. 1, pp. 96-109, 2009.

[6] Y. Liu, N. Tuleouva, E. Ramanculov, and A. Revzin, "Aptamer-based electrochemical biosensor for interferon gamma detection," *Analytical chemistry,* vol. 82, no. 19, pp. 8131-8136, 2010.

[7] A. Minopoli *et al.*, "Ultrasensitive antibody-aptamer plasmonic biosensor for malaria biomarker detection in whole blood," *Nature communications,* vol. 11, no. 1, pp. 1-10, 2020.

[8] M. T. Hwang *et al.*, "Ultrasensitive detection of nucleic acids using deformed graphene channel field effect biosensors," *Nature communications,* vol. 11, no. 1, pp. 1-11, 2020.

[9] D. Amsen, K. E. de Visser, and T. Town, "Approaches to determine expression of inflammatory cytokines," in *Inflammation and Cancer*: Springer, 2009, pp. 107-142.

[10] H. O. Kim, H.-S. Kim, J.-C. Youn, E.-C. Shin, and S. Park, "Serum cytokine profiles in healthy young and elderly population assessed using multiplexed bead-based immunoassays," *Journal of translational medicine,* vol. 9, no. 1, pp. 1-7, 2011.

[11] M. M. Imani, M. Sadeghi, H. Khazaie, M. Emami, D. Sadeghi Bahmani, and S. Brand, "Serum and Plasma Tumor Necrosis Factor Alpha Levels in Individuals with Obstructive Sleep Apnea Syndrome: A Meta-Analysis and Meta-Regression," *Life,* vol. 10, no. 6, p. 87, 2020.

[12] D. Sarkar, W. Liu, X. Xie, A. C. Anselmo, S. Mitragotri, and K. Banerjee, "MoS_2 field-effect transistor for next-generation label-free biosensors," *ACS nano,* vol. 8, no. 4, pp. 3992-4003, 2014.

[13] S. Ghosh, D. Datta, S. Chaudhry, M. Dutta, and M. A. Stroscio, "Rapid detection of tumor necrosis factor-alpha using quantum dot-based optical aptasensor," *IEEE transactions on nanobioscience,* vol. 17, no. 4, pp. 417-423, 2018.

[14] C. Yao, Y. Qi, Y. Zhao, Y. Xiang, Q. Chen, and W. Fu, "Aptamer-based piezoelectric quartz crystal microbalance biosensor array for the quantification of IgE," *Biosensors and Bioelectronics,* vol. 24, no. 8, pp. 2499-2503, 2009.

[15] Y.-K. Bahk, H.-H. Kim, D.-S. Park, S.-C. Chang, and J.-S. Go, "A new concept for efficient sensitivity amplification of a QCM based immunosensor for TNF-α by using modified magnetic particles under applied magnetic field," *Bulletin of the Korean Chemical Society,* vol. 32, no. 12, pp. 4215-4220, 2011.

[16] C. Jiang, Q. Li, J. Huang, S. Bi, R. Ji, and Q. Guo, "Single-layer MoS_2 mechanical resonant piezo-sensors with high mass sensitivity," *ACS Applied Materials & Interfaces,* vol. 12, no. 37, pp. 41991-41998, 2020.

[17] S. M. Ahmed and H. Gerischer, "Influence of crystal surface orientation on redox reactions at semiconducting MoS_2," *Electrochimica Acta,* vol. 24, no. 6, pp. 705-711, 1979.

[18] S. Su *et al.*, "Dual-target electrochemical biosensing based on DNA structural switching on gold nanoparticle-decorated MoS_2 nanosheets," *ACS applied materials & interfaces,* vol. 8, no. 11, pp. 6826-6833, 2016.

[19] M. Bahri, A. Baraket, N. Zine, M. B. Ali, J. Bausells, and A. Errachid, "Capacitance electrochemical biosensor based on silicon nitride transducer for TNF-α cytokine detection in artificial human saliva: Heart failure (HF)," *Talanta,* vol. 209, p. 120501, 2020.

[20] A. Liu *et al.*, "An ultrasensitive photoelectrochemical immunosensor by integration of nanobody, TiO2 nanorod arrays and ZnS nanoparticles for the detection of tumor necrosis factor-α," *Journal of Electroanalytical Chemistry,* vol. 803, pp. 1-10, 2017.

[21] K. Arkusz and E. Paradowska, "Impedimetric Detection of Femtomolar Levels of Interleukin 6, Interleukin 8, and Tumor Necrosis Factor Alpha Based on Thermally Modified Nanotubular Titanium Dioxide Arrays," *Nanomaterials,* vol. 10, no. 12, p. 2399, 2020.

[22] Z. Hao *et al.*, "Measurement of cytokine biomarkers using an aptamer-based affinity graphene nanosensor on a flexible substrate toward wearable applications," *Nanoscale,* vol. 10, no. 46, pp. 21681-21688, 2018.

[23] Z. Wang *et al.*, "An ultraflexible and stretchable aptameric graphene nanosensor for biomarker detection and monitoring," *Advanced functional materials,* vol. 29, no. 44, p. 1905202, 2019.

[24] M.-Z. Li, S.-T. Han, and Y. Zhou, "Recent Advances in Flexible Field-Effect Transistors toward Wearable Sensors," *Advanced Intelligent Systems,* vol. 2, no. 11, p. 2000113, 2020.

[25] K. Cho *et al.*, "Electric stress-induced threshold voltage instability of multilayer MoS_2 field effect transistors," *ACS nano,* vol. 7, no. 9, pp. 7751-7758, 2013.

[26] H. Nam *et al.*, "Multiple MoS 2 transistors for sensing molecule interaction kinetics," *Scientific reports,* vol. 5, no. 1, pp. 1-13, 2015.

[27] Y. Dong *et al.*, "Insights into the Crystallinity of Layer-Structured Transition Metal Dichalcogenides on Potassium Ion Battery Performance: A Case Study of Molybdenum Disulfide," *Small,* vol. 15, no. 15, p. 1900497, 2019.

[28] L. Wu, E. Xiong, X. Zhang, X. Zhang, and J. Chen, "Nanomaterials as signal amplification elements in DNA-based electrochemical sensing," *Nano Today,* vol. 9, no. 2, pp. 197-211, 2014.

[29] W. Wen *et al.*, "Recent advances in emerging 2D nanomaterials for biosensing and bioimaging applications," *Materials Today,* vol. 21, no. 2, pp. 164-177, 2018.

[30] A. Bolotsky *et al.*, "Two-dimensional materials in biosensing and healthcare: from in vitro diagnostics to optogenetics and beyond," *ACS nano,* vol. 13, no. 9, pp. 9781-9810, 2019.

[31] N. Aroonyadet *et al.*, "Highly scalable, uniform, and sensitive biosensors based on top-down indium oxide nanoribbons and electronic enzyme-linked immunosorbent assay," *Nano letters,* vol. 15, no. 3, pp. 1943-1951, 2015.

[32] L. Wang, K. Jiang, and G. Shen, "A perspective on flexible sensors in developing diagnostic devices," *Applied Physics Letters,* vol. 119, no. 15, p. 150501, 2021.

[33] A. Takemoto *et al.*, "Printable transparent microelectrodes toward mechanically and visually imperceptible electronics," *Advanced Intelligent Systems,* vol. 2, no. 11, p. 2000093, 2020.

[34] S. A. Han *et al.*, "Point-defect-passivated MoS_2 nanosheet-based high performance piezoelectric nanogenerator," *Advanced Materials,* vol. 30, no. 21, p. 1800342, 2018.

[35] P. Fathi-Hafshejani *et al.*, "Two-dimensional-material-based field-effect transistor biosensor for detecting COVID-19 Virus (SARS-CoV-2)," *ACS nano,* vol. 15, no. 7, pp. 11461-11469, 2021.

[36] R. A. Potyrailo, R. C. Conrad, A. D. Ellington, and G. M. Hieftje, "Adapting selected nucleic acid ligands (aptamers) to biosensors," *Analytical Chemistry,* vol. 70, no. 16, pp. 3419-3425, 1998.

[37] S. Balamurugan, A. Obubuafo, S. A. Soper, and D. A. Spivak, "Surface immobilization methods for aptamer diagnostic applications," *Analytical and bioanalytical chemistry,* vol. 390, no. 4, pp. 1009-1021, 2008.

[38] S. L. Clark and V. T. Remcho, "Electrochromatographic retention studies on a flavin-binding RNA aptamer sorbent," *Analytical chemistry,* vol. 75, no. 21, pp. 5692-5696, 2003.

[39] D. Hiller *et al.*, "Low temperature silicon dioxide by thermal atomic layer deposition: Investigation of material properties," *Journal of Applied Physics,* vol. 107, no. 6, p. 064314, 2010.

[40] S. Arshavsky-Graham *et al.*, "Aptamers vs. antibodies as capture probes in optical porous silicon biosensors," *Analyst,* vol. 145, no. 14, pp. 4991-5003, 2020.

[41] E. M. McConnell, J. Nguyen, and Y. Li, "Aptamer-based biosensors for environmental monitoring," *Frontiers in chemistry,* vol. 8, p. 434, 2020.

[42] K. Han, Z. Liang, and N. Zhou, "Design strategies for aptamer-based biosensors," *Sensors,* vol. 10, no. 5, pp. 4541-4557, 2010.

[43] C. Roxo, W. Kotkowiak, and A. Pasternak, "G-quadruplex-forming aptamers—characteristics, applications, and perspectives," *Molecules,* vol. 24, no. 20, p. 3781, 2019.

[44] S. D. Jayasena, "Aptamers: an emerging class of molecules that rival antibodies in diagnostics," *Clinical chemistry,* vol. 45, no. 9, pp. 1628-1650, 1999.

[45] E. W. Orava, N. Jarvik, Y. L. Shek, S. S. Sidhu, and J. Gariépy, "A short DNA aptamer that recognizes TNFα and blocks its activity in vitro," *ACS chemical biology,* vol. 8, no. 1, pp. 170-178, 2013.

[46] J. Wang, G. Li, and L. Li, "Synthesis strategies about 2D materials," *Two-Dimensional Materials—Synthesis, Characterization and Potential Applications; Nayak, PK, Ed,* pp. 1-20, 2016.

[47] Y. H. Lee *et al.*, "Synthesis of large-area MoS_2 atomic layers with chemical vapor deposition," *Advanced materials,* vol. 24, no. 17, pp. 2320-2325, 2012.

[48] Y.-H. Lee *et al.*, "Synthesis and transfer of single-layer transition metal disulfides on diverse surfaces," *Nano letters,* vol. 13, no. 4, pp. 1852-1857, 2013.

[49] A. M. Van Der Zande *et al.*, "Grains and grain boundaries in highly crystalline monolayer molybdenum disulphide," *Nature materials,* vol. 12, no. 6, pp. 554-561, 2013.

[50] M. Yi and Z. Shen, "A review on mechanical exfoliation for the scalable production of graphene," *Journal of Materials Chemistry A,* vol. 3, no. 22, pp. 11700-11715, 2015.

[51] H. Li, J. Wu, Z. Yin, and H. Zhang, "Preparation and applications of mechanically exfoliated single-layer and multilayer MoS_2 and WSe_2 nanosheets," *Accounts of chemical research,* vol. 47, no. 4, pp. 1067-1075, 2014.

[52] R. F. M. Lobo, M. A. Pereira-da-Silva, M. Raposo, R. M. Faria, and O. N. Oliveira Jr, "In situ thickness measurements of ultra-thin multilayer polymer films by atomic force microscopy," *Nanotechnology,* vol. 10, no. 4, p. 389, 1999.

[53] X. Yao, M. Jericho, D. Pink, and T. Beveridge, "Thickness and elasticity of gram-negative murein sacculi measured by atomic force microscopy," *Journal of bacteriology,* vol. 181, no. 22, pp. 6865-6875, 1999.

[54] A. How, "AM-FM Viscoelastic mapping mode."

[55] P. Nemes-Incze, Z. Osváth, K. Kamarás, and L. P. Biró, "Anomalies in thickness measurements of graphene and few layer graphite crystals by tapping mode atomic force microscopy," *Carbon,* vol. 46, no. 11, pp. 1435-1442, 2008.

[56] W. Melitz, J. Shen, A. C. Kummel, and S. Lee, "Kelvin probe force microscopy and its application," *Surface science reports,* vol. 66, no. 1, pp. 1-27, 2011.

[57] J. R. Lakowicz, *Principles of fluorescence spectroscopy*. Springer science & business media, 2013.

[58] I. Agreatermeasureofconf, "the Model 4200-SCS."

[59] M. Magnozzi *et al.*, "Local Optical Properties in CVD-Grown Monolayer WS_2 Flakes," *The Journal of Physical Chemistry C,* vol. 125, no. 29, pp. 16059-16065, 2021.

[60] G. Seo *et al.*, "Rapid detection of COVID-19 causative virus (SARS-CoV-2) in human nasopharyngeal swab specimens using field-effect transistor-based biosensor," *ACS nano,* vol. 14, no. 4, pp. 5135-5142, 2020.

[61] S. M. George, "Atomic layer deposition: an overview," *Chemical reviews,* vol. 110, no. 1, pp. 111-131, 2010.

[62] A. E. Marquardt, E. M. Breitung, T. Drayman-Weisser, G. Gates, and R. J. Phaneuf, "Protecting silver cultural heritage objects with atomic layer deposited corrosion barriers," *Heritage science,* vol. 3, no. 1, pp. 1-12, 2015.

[63] C. Zhou, S. Raju, B. Li, M. Chan, Y. Chai, and C. Y. Yang, "Self-driven metal–semiconductor–metal WSe_2 photodetector with asymmetric contact geometries," *Advanced Functional Materials,* vol. 28, no. 45, p. 1802954, 2018.

[64] W. Gao *et al.*, "2D WS_2 Based Asymmetric Schottky Photodetector with High Performance," *Advanced Electronic Materials,* vol. 7, no. 7, p. 2000964, 2021.

[65] J. Lu *et al.*, "An asymmetric contact-induced self-powered 2D In 2 S 3 photodetector towards high-sensitivity and fast-response," *Nanoscale,* vol. 12, no. 13, pp. 7196-7205, 2020.

[66] M. Miansari, J. R. Friend, and L. Y. Yeo, "Enhanced ion current rectification in 2D graphene-based nanofluidic devices," *Advanced Science,* vol. 2, no. 6, p. 1500062, 2015.

[67] P. Bampoulis, R. van Bremen, Q. Yao, B. Poelsema, H. J. W. Zandvliet, and K. Sotthewes, "Defect dominated charge transport and fermi level pinning in MoS_2/metal contacts," *ACS applied materials & interfaces,* vol. 9, no. 22, pp. 19278-19286, 2017.

[68] A. Sebastian, R. Pendurthi, T. H. Choudhury, J. M. Redwing, and S. Das, "Benchmarking monolayer MoS 2 and WS 2 field-effect transistors," *Nature communications,* vol. 12, no. 1, pp. 1-12, 2021.

[69] J. T. Ye, Y. J. Zhang, R. Akashi, M. S. Bahramy, R. Arita, and Y. Iwasa, "Superconducting dome in a gate-tuned band insulator," *Science,* vol. 338, no. 6111, pp. 1193-1196, 2012.

[70] Y. Zhang, J. Ye, Y. Matsuhashi, and Y. Iwasa, "Ambipolar MoS_2 thin flake transistors," *Nano letters,* vol. 12, no. 3, pp. 1136-1140, 2012.

[71] J. K. Farney, L. K. Mamedova, B. H. Godsey, and B. J. Bradford, "Validation of an ELISA for measurement of tumor necrosis factor alpha in bovine plasma," *Journal of dairy science,* vol. 94, no. 7, pp. 3504-3509, 2011.

[72] K. Shah and P. Maghsoudlou, "Enzyme-linked immunosorbent assay (ELISA): the basics," *British journal of hospital medicine,* vol. 77, no. 7, pp. C98-C101, 2016.

[73] R. Say, S. E. Diltemiz, S. Çelik, and A. Ersöz, "Nanolabel for TNF-α determination," *Applied surface science,* vol. 275, pp. 233-238, 2013.

[74] R. Say, E. B. Özkütük, Ö. B. Ünlüer, D. Uğurağ, and A. Ersöz, "Nano anti-tumor necrosis factor-alpha based potentiometric sensor for tumor necrosis factor-alpha detection," *Sensors and Actuators B: Chemical,* vol. 209, pp. 864-869, 2015.

[75] Y. Liu, Z. Matharu, A. Rahimian, and A. Revzin, "Detecting multiple cell-secreted cytokines from the same aptamer-functionalized electrode," *Biosensors and Bioelectronics,* vol. 64, pp. 43-50, 2015.

[76] T. Kwa *et al.*, "Reconfigurable microfluidics with integrated aptasensors for monitoring intercellular communication," *Lab on a Chip,* vol. 14, no. 10, pp. 1695-1704, 2014.

[77] M. S. Luchansky and R. C. Bailey, "Rapid, multiparameter profiling of cellular secretion using silicon photonic microring resonator arrays," *Journal of the American Chemical Society,* vol. 133, no. 50, pp. 20500-20506, 2011.

[78] Y. Liu, Q. Zhou, and A. Revzin, "An aptasensor for electrochemical detection of tumor necrosis factor in human blood," *Analyst,* vol. 138, no. 15, pp. 4321-4326, 2013.

[79] Z. Wang, Z. Hao, S. Yu, C. Huang, Y. Pan, and X. Zhao, "A wearable and deformable graphene-based affinity nanosensor for monitoring of cytokines in biofluids," *Nanomaterials,* vol. 10, no. 8, p. 1503, 2020.

[80] J. Zhu *et al.*, "An integrated adipose-tissue-on-chip nanoplasmonic biosensing platform for investigating obesity-associated inflammation," *Lab on a Chip,* vol. 18, no. 23, pp. 3550-3560, 2018.

[81] C. Jiang, M. T. Alam, S. M. Silva, S. Taufik, S. Fan, and J. J. Gooding, "Unique sensing interface that allows the development of an electrochemical immunosensor for the detection of tumor necrosis factor α in whole blood," *ACS sensors,* vol. 1, no. 12, pp. 1432-1438, 2016.

[82] H. Wei, S. Ni, C. Cao, G. Yang, and G. Liu, "Graphene oxide signal reporter based multifunctional immunosensing platform for amperometric profiling of multiple cytokines in serum," *ACS sensors,* vol. 3, no. 8, pp. 1553-1561, 2018.

[83] A. K. Yagati, G.-Y. Lee, S. Ha, K.-A. Chang, J.-C. Pyun, and S. Cho, "Impedimetric tumor necrosis factor-α sensor based on a reduced graphene oxide nanoparticle-modified electrode array," *Journal of Nanoscience and Nanotechnology,* vol. 16, no. 11, pp. 11921-11927, 2016.

[84] L. Barhoumi *et al.*, "A novel chronoamperometric immunosensor for rapid detection of TNF-α in human saliva," *Sensors and Actuators B: Chemical,* vol. 266, pp. 477-484, 2018.

[85] A. Di Bartolomeo *et al.*, "Asymmetric Schottky contacts in bilayer MoS_2 field effect transistors," *Advanced Functional Materials,* vol. 28, no. 28, p. 1800657, 2018.

[86] A. Hasani *et al.*, "Direct synthesis of two-dimensional MoS 2 on p-type Si and application to solar hydrogen production," *NPG Asia Materials,* vol. 11, no. 1, pp. 1-9, 2019.